Validation of subgrain-size piezometry as a tool for measuring stress in polymineralic rocks

Rellie M. Goddard[1*], Kathryn M. Kumamoto[2], Lars N. Hansen[3], David Wallis[4], Andrew J. Cross[1], and Christopher A. Thom[5]

[1]Department of Geology and Geophysics, Woods Hole Oceanographic Institution, Woods Hole, MA, USA
[2]Lawrence Livermore National Laboratory, Livermore, CA, USA
[3]Department of Earth and Environmental Sciences, University of Minnesota, Minneapolis, MN, USA
[4]Department of Earth Sciences, University of Cambridge, Cambridge, UK
[5]Rhenium Alloys, Inc., North Ridgeville, OH, USA

Key Points:

- Subgrain sizes are insensitive to the presence of secondary phases in polymineralic rocks.
- The grain size of a rock influences what portion of the deformation history the subgrain size records.
- Stresses estimated from individual phases in a mixture do not necessarily record the bulk stress applied to the rock.

[*]Current address, Department of Earth, Environmental and Geographic Sciences, The University of British Columbia, 4237 University Way, Kelowna, BC V1V 1V7, Canada

Corresponding author: Rellie M. Goddard, rellie.goddard@gmail.com

Abstract

We deformed samples with varied proportions of olivine and orthopyroxene in a deformation-DIA apparatus to test the applicability of subgrain-size piezometry to polymineralic rocks. We measured the stress within each phase *in situ* via X-ray diffraction during deformation at a synchrotron beamline. Subgrain-size piezometry was subsequently applied to the recovered samples to estimate the stress that each phase supported during deformation. For olivine, the final *in-situ* stresses are consistent with the stresses estimated via subgrain-size piezometry, both in monomineralic and polymineralic samples, despite non-steady state conditions. However, stress estimates from subgrain-size piezometry do not reliably record the *in-situ* stress in samples with grain sizes that are too small for extensive subgrain-boundary formation. For orthopyroxene, subgrain boundaries are typically sparse due to the low strains attained by orthopyroxene in olivine-orthopyroxene mixtures. Where sufficient substructure does exist, our data supports the use of the subgrain-size piezometer on orthopyroxene. These results do, however, suggest that care should be taken when applying subgrain-size piezometry to strong minerals that may have experienced little strain. Stresses estimated by X-ray diffraction also offer insight into stress partitioning between phases. In mixtures deformed at mean stresses > 5 GPa, orthopyroxene supports stresses greater than those supported by olivine. This stress partitioning is consistent with established theory that predicts a slightly higher stress within a 'strong' phase contained in a material consisting of interconnected weak layers. Overall, these results demonstrate that subgrain-size piezometry is a valuable tool for quantifying the stress state of polymineralic rocks.

Plain Language Summary

To measure the stresses previously supported by exhumed lower-crustal and upper-mantle rocks, we rely on examining features in the rocks that have a calibrated relationship with stress. One such metric is based on the size of subgrains, which are distinct crystallographic regions within individual grains that comprise a rock. Experiments on rocks composed of a single mineral have shown the subgrain size to have an inverse relationship with stress. However, the majority of rocks are composed of multiple minerals. In addition, subgrain sizes generated in the experiments used in the calibrations each record a single, steady-state stress, whereas natural rocks are often subject to complex stress histories.

We test the applicability of using subgrain size to estimate stress in rocks containing more than one mineral through high-temperature, high-pressure experiments paired with *in-situ* X-ray diffraction. Results indicate that stresses estimated from subgrain sizes in rocks composed of more than one mineral are a good indication of the final stress experienced by a sample regardless of the deformation history. However, additional parameters, such as the amount of strain and the grain size relative to the subgrain size, need to be considered when applying this method to natural rocks.

1 Introduction

Paleostress estimates from exhumed rocks provide critical insight into the mechanical state of Earth's lithosphere (e.g., Kohlstedt & Weathers, 1980), strain localisation along plate boundaries (e.g., Ambrose et al., 2018; Boutonnet et al., 2013), and elastic loading of the mid-crust through the earthquake cycle (e.g., Trepmann & Seybold, 2019). Such stresses can be estimated via paleopiezometry, that is, the relationship between stress and specific microstructural features (e.g., Nicolas, 1978; Tullis, 1979). The most widely implemented paleopiezometer is based on the mean size of dynamically recrystallised grains, which follows an inverse power law with differential stress in monomineralic rocks (e.g., Karato et al., 1980; Luton & Sellars, 1969; Shimizu, 2008; Stipp & Tullis, 2003; Twiss, 1986). However, grain sizes in a polymineralic rock can be influenced by the presence of secondary phases that pin migrating grain boundaries (Cross & Skemer, 2017; Evans et al., 2001; Hiraga et al., 2010; Smith, 1948; Tasaka et al., 2017). Consequently, grain-size piezometry tends to overestimate paleostresses when applied to well-mixed polymineralic rocks (e.g., Hansen & Warren, 2015).

An alternative proxy for paleostress in polymineralic rocks is subgrain size (Twiss, 1986). Subgrains are crystallographic regions enclosed by low-angle (typically < 10–$15°$) boundaries within individual grains (Karato, 2012, page 94). As with grain size, an inverse relationship exists between differential stress and the spacing of subgrain boundaries (e.g., Durham et al., 1977; Karato et al., 1980; Raleigh & Kirby, 1970; Servi et al., 1952; Toriumi, 1979). However, subgrain-size piezometry offers three potential advantages over grain-size piezometry. First, low-angle boundaries have lower mobilities than grain boundaries (e.g., Huang et al., 2000) and are therefore more resistant to post-kinematic static annealing (Qin et al., 2003). Second, mean subgrain sizes exhibit the same relationship with stress in both relict and recrystallized grains (see Figure 8 in Ross et al., 1980, and Figure 6 in Trimby

et al., 1998) meaning no distinction is required between the two grain populations. Finally, for a given stress, subgrain size is thought to be unaffected by the presence of secondary minerals (Hansen & Warren, 2015; White, 1979).

Recently Goddard et al. (2020) calibrated a new subgrain-size piezometer using electron backscatter diffraction (EBSD), a widely used technique for characterising microstructural features. This new piezometer was calibrated using both olivine and quartz, resulting in a generalised relationship that could potentially be applied to other minerals without the need for additional calibration. Subgrain size therefore provides a powerful tool for estimating stress from natural polymineralic rocks. Nevertheless, two key uncertainties remain. First, although subgrain sizes should be unaffected by the presence of secondary phases as they are intragranular features (Hansen & Warren, 2015; White, 1979), no study has directly tested this idea. Second, it is unclear how subgrain size relates to stress under non-steady-state conditions. Nearly all piezometers are calibrated using experiments in which stress has reached a steady state (e.g., Karato et al., 1980; Stipp & Tullis, 2003), and thus the statistics of microstructural features are likewise assumed to be invariant with further strain. Recent work has been conducted to explore how grain size responds to changes in stress (e.g., Kidder et al., 2016; Soleymani et al., 2020), however, the equivalent published work on subgrain-size piezometry is limited and inconclusive. As natural rocks often undergo significant stress changes, for example during exhumation (Behr & Platt, 2011) or during the seismic cycle (e.g., Campbell & Menegon, 2019; Menegon et al., 2021), understanding how subgrain sizes respond to changing stresses is vital to accurately interpreting the rock record.

To address these questions, we conducted experiments on synthetic polymineralic samples of olivine and orthopyroxene using a deformation-DIA (D-DIA) apparatus at beamline 6-BM-B of the Advanced Photon Source synchrotron, Argonne National Laboratory, Illinois. To explore the extent to which subgrain size tracks stress in non-steady-state systems, we incorporated temperature and strain-rate steps into most experiments. We compared stresses measured *in situ* via X-ray diffraction to those estimated from EBSD maps of recovered samples and the subgrain-size piezometer of Goddard et al. (2020). In addition, we explored how stress partitioning between phases in the polymineralic aggregates compared to Handy's (1994) model for two-phase flow.

Our results support the hypothesis that subgrain sizes are unaffected by the presence of secondary phases. The stresses estimated from subgrain-size piezometry are consistent with the final stresses measured *in-situ*, irrespective of the stress histories that preceded them. Stress partitioning within individual phases is also found to be consistent with that expected from models of like microstructures. As such, this study broadens the applicability of subgrain-size piezometry to polymineralic natural rocks. However, we also caution that careful consideration should be taken when using the subgrain-size piezometer to infer the bulk strength of polymineralic rocks, especially in low-strain or fine-grained samples.

2 Methods

2.1 Sample Synthesis

D-DIA experiments consisted of a stack of two samples deformed in series. Figure 1 illustrates a typical sample assembly. One of the samples was commonly olivine, which was used as a stress sensor in the experiments. Given the use of olivine to calibrate the original subgrain-size piezometer, these monomineralic samples were also used as a control when comparing stress measurements from X-ray diffraction to those from piezometry. Other samples consisted of olivine orthopyroxenite or harzburgite, which contained 85 vol.% and 30 or 50 vol.% of orthopyroxene, respectively.

Samples were synthesised either at Brown University or the University of Minnesota. LT-DrySC, a dry olivine sample, was synthesised at Brown University from San Carlos olivine with particle sizes 10–32 µm. This dry olivine was made from a 'wet olivine', which had ∼0.5–0.7 wt% deionised water added to the olivine powder prior to hot pressing. Powders were sealed in a nickel jacket and hot pressed at a confining pressure of 1.3 GPa and temperature of 900°C for 24–26 hours in a triaxial, Tullis-modified Griggs apparatus, using solid NaCl as the confining medium. To dehydrate, the sample was placed in a 1 atm CO/CO_2 furnace at 1000°C and a P_{O_2} of $\sim 10^{-10}$ atm for 10 hours.

At the University of Minnesota, samples were synthesised from powders of Bamble enstatite and San Carlos olivine, with particle sizes < 10 µm. For samples 33 and PT-1166, powders of olivine were combined with 1% enstatite to buffer the silica activity. For sample PT-1299HiFe, enstatite was mixed in ethanol with olivine powder in a 30:70 ratio. For PI-2056, powders of enstatite and pure olivine were similarly prepared, as well as 50:50 and

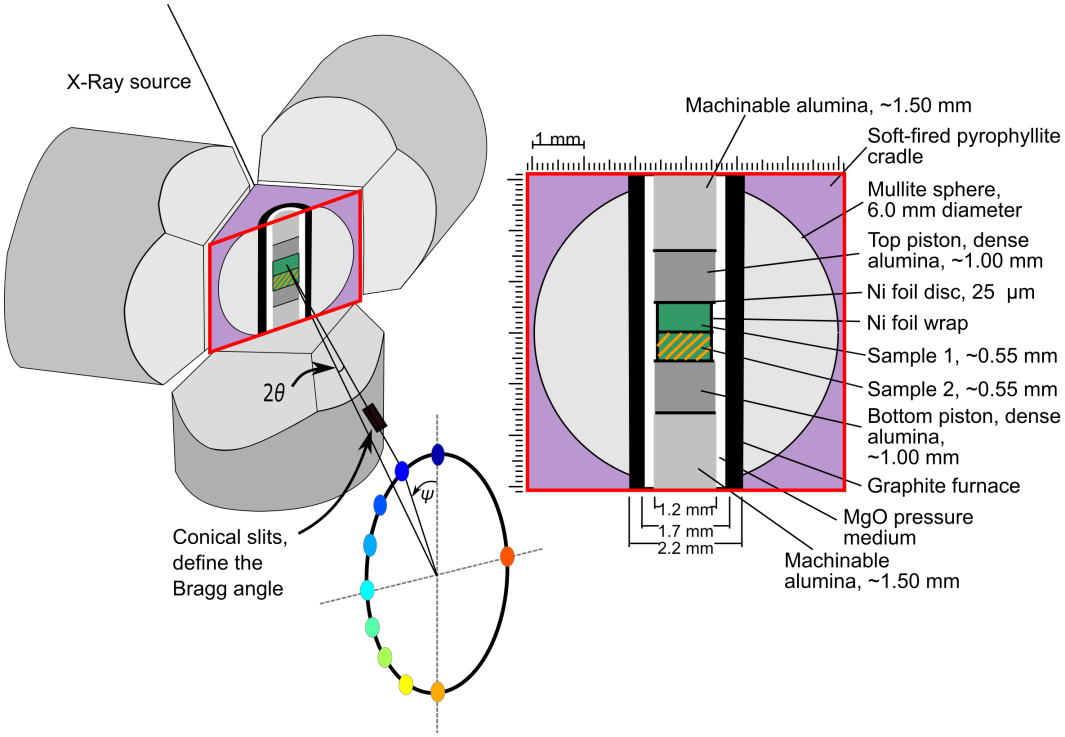

Figure 1. Schematic illustration of a typical D-DIA sample assembly, modified from Durham et al. (2002) and Hansen et al. (2019).

85:15 ratios of enstatite to olivine. Powders were tumbled for at least 12 hours in a plastic bottle with plastic-coated iron balls and subsequently dried on a hot plate at 60°C until all the ethanol had evaporated. Powders were then placed in a 1 atm CO/CO_2 furnace, with a P_{O_2} of $\sim 10^{-10}$ atm, in which temperature was ramped up to 1000°C over 10 hours and then held constant for 12 hours before cooling. The sample powders were cold pressed at ~100 MPa into a Ni can on top of a layer of NiO powder, which was present to buffer oxygen fugacity. For sample PI-2056, the cold press consisted of roughly equal layers of the aforementioned different compositional ratios. Samples were vacuum hot-pressed in a gas-medium apparatus at a vacuum pressure on the interior of the jacket of ~10 Pa and at a confining pressure of 300 MPa (Meyers et al., 2017). Hot presses were carried out at 1250°C under a small uniaxial load (~1 MPa) to aid compaction. For PT-1299HiFe and PI-2056, the hot press was continued until compaction effectively ceased, which took between 0.5 and 1.3 hours. Samples 33 and PT-1166 were part of a series that were hot-pressed for between 3 and 60 hours to produce different grain sizes.

2.2 Sample Assembly

Hot presses were cored using a diamond coring drill to produce right-cylindrical samples of diameters 1.05–1.19 mm, which were subsequently ground to a height of 0.55±0.05 mm. For each experiment, a pair of samples were stacked between dense alumina pistons and then machinable alumina. Discs of nickel foil were placed between each component within the assembly to act as strain markers and also control the oxygen fugacity at the Ni/NiO buffer. The circumference of the samples was also wrapped in Ni foil. The assembly stack was placed within concentric sleeves of MgO and graphite, which provided an insulator and a resistive heater, respectively (See Figure 1). All components were placed inside a mullite sphere, which acted as the solid confining medium, itself residing within a pyrophyllite cube. The pyrophyllite cells were soft-fired for 3 hours at 900°C prior to sample assembly, which enabled them to flow during initial compression to form a gasket between the six anvil cells. Completed assemblies were sealed using a zirconia cement, ground to be square, and then left in an oven at ∼120°C for $\geq$ 2 hours to ensure an anhydrous state.

2.3 Experimental Procedure

We generated the desired stress state in the sample in the same manner as previous investigations implementing D-DIA experiments (Durham et al., 2009; Mei et al., 2010; Wang et al., 2003; Weidner et al., 2010). Pressure was applied to the pyrophyllite assembly cube through a hydraulically-loaded anvil in contact with each cube face. Pressurisation from the main loading ram applied equal load to all six anvils simultaneously, generating a hydrostatic compressive stress. Temperature was controlled using a calibrated relationship with heater power, as the inclusion of a thermocouple tends to degrade the mechanical stability of the sample assembly (Dixon & Durham, 2018). Once target pressures, here equivalent to mean stress ($(\sigma_v+2\sigma_h)/3$), and temperatures were reached, differential stress was generated by independently advancing the vertical anvils, each controlled by driving a hydraulic syringe pump at a constant rate. Due to compressibility of the syringe fluid, the experimental boundary conditions are neither truly constant strain rate nor constant load. Moreover, changes in heater power (i.e., temperature) led to minor changes in the strain rate of the sample during an experiment. Nevertheless, nominally constant strain rates were reached after an initial loading phase. Meanwhile, the main ram was servo controlled to maintain a nominally constant mean stress (Durham et al., 2002).

During each experiment, a high-energy, white X-ray source was used to provide *in-situ* stress and strain measurements via energy-dispersive X-ray diffraction and X-ray radiography, respectively. Ten solid-state detectors were arranged downstream of the sample at a variety of fixed azimuths (ψ) and at an angle of 6.5° (2θ) to the beam direction (Figure 1). The Bragg angle of 6.5° was fixed through the use of conical slits and provided a collimated signal that ensured X-rays arriving at the detectors were diffracted from within the sample, and not from the surrounding assembly components. Each analysed peak within the diffraction spectrum corresponds to an $\{hkl\}$ plane whose atomic spacing, or '*d*-spacing', was calculated through Bragg's law and the fixed diffraction angle. This energy-to-*d*-spacing conversion, as well as the Bragg angle, was calibrated at least once every seven experiments (typically every two days) using an alumina-powder standard.

Diffraction spectra were collected, alternating between the top and the bottom samples, for durations of 20 to 60 seconds depending on the clarity of the peaks. Peaks used in this analysis are highlighted in Figure 2 and correspond to the {130}, {131}, and {112} planes in olivine and the {421}, {610}, and {321} planes in orthopyroxene.

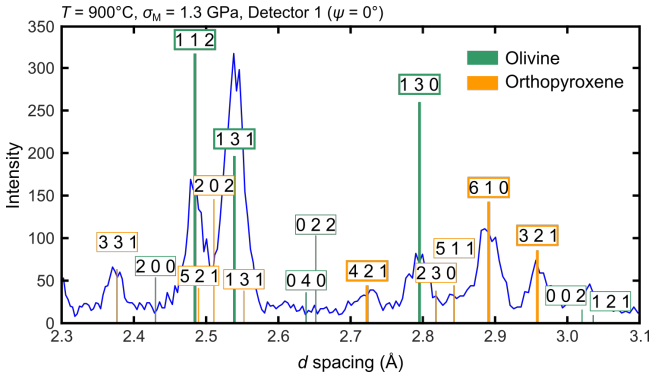

Figure 2. X-ray diffraction spectrum collected for 20 seconds in a harzburgite sample. The measured data are plotted as a blue line. Green and orange lines represent key diffracting planes in olivine and orthopyroxene, respectively. Peak labels outlined in bold are those used to measure stress in this experimental series.

Mean stress and differential stress were calculated from the measured d-spacing of $\{hkl\}$ peaks following previous work (e.g., Durham et al., 2009; Hansen et al., 2019; Mei et al., 2010; Wang et al., 2013; Weidner et al., 2010). Mean stress (P) was measured from the {130} peak of olivine, calculated using the third-order Birch-Murnaghan equation of state for olivine,

$$P = \left(\frac{3\left(K_0 + K_{\mathrm{T}}^{'}\triangle T\right)}{2}\right)\left[\left(\frac{V_{0,\mathrm{T}}}{V}\right)^{\frac{7}{3}} - \left(\frac{V_{0,\mathrm{T}}}{V}\right)^{\frac{5}{3}}\right]\left\{1 + \frac{3}{4}\left(K_{\mathrm{P}}^{'} - 4\right)\left[\left(\frac{V_{0,\mathrm{T}}}{V}\right)^{\frac{2}{3}} - 1\right]\right\}, \tag{1}$$

where ΔT is the difference in temperature relative to the temperature at which the thermal expansion measurements were made, K_0 is the bulk modulus and K'_{T} and K'_{P} are the temperature and pressure derivatives of K_0, respectively. Values of 129.4 GPa for K_0 and 4.29 for K'_{P} were taken from Abramson et al. (1997). For K'_{T}, a value of -0.0224 GPa K^{-1} was taken from Kumazawa and Anderson (1969). The unit-cell volume, V, was calculated for each diffraction pattern during the experiment through

$$V = \left[d_{\mathrm{p}}\left(h^2 + k^2 + l^2\right)^{\frac{1}{2}}\right]^3, \tag{2}$$

where $d_{\mathrm{p}} = \frac{d_{\mathrm{v}} + 2d_{\mathrm{h}}}{3}$, d_{v} is the d-spacing measured at the vertical azimuth, and d_{h} is the d-spacing measured at the horizontal azimuth. To calculate d_{h} and d_{v}, d-spacing was plotted against ψ and then a sine wave was fit to the data. d_{h} and d_{v} were taken to be the maximum and minimum of the sine wave, which sit 90° apart. $V_{0,\mathrm{T}}$ is the unit-cell volume at the experiment temperature and ambient pressure, and is calculated as

$$V_{0,\mathrm{T}} = V_0 \mathrm{exp}\left(2.55 \times 10^{-5} \times (T - T_0) + \frac{1}{2} \times 1.15 \times 10^{-8} \times \left(T^2 - T_0^2\right)\right), \tag{3}$$

where V_0 is the unit-cell volume at ambient temperature and pressure, T is the temperature, and T_0 is the temperature at which the measurements of thermal expansion were made.

Differential stress, σ, was calculated using the difference in d-spacing between the horizontal and vertical directions,

$$\sigma = \left(\frac{1}{2G_{\mathrm{R}}}\right)^{-1}\frac{d_{\mathrm{h}} - d_{\mathrm{v}}}{d_{\mathrm{p}}}, \tag{4}$$

where G_{R} is the X-ray shear modulus calculated assuming the Reuss (isostress) condition (Singh et al., 1998) and using the elastic constants from Abramson et al. (1997) and Isaak (1992).

Prior to fitting peaks in the diffraction data, the intensity spectra were smoothed using a Savitzky-Golay filter and interpolated with a spline function. Due to the complicated diffraction patterns present in mixtures of olivine and orthopyroxene, peak locations were identified by fitting Gaussians to the highest intensity portions of each individual peak, rather than by fitting a mixing model of multiple Gaussians. When compared to the peak-fitting model (peakfit.m, O'Haver, 2018, page 340–358) used by Hansen et al. (2019) on a representative set of diffraction patterns for monophase olivine, stress and mean stress measurements were similar.

Axial strain was obtained by using digital image cross-correlation to precisely measure the positions of the nickel-foil strain markers in X-ray radiographs. By applying this technique, we were able to resolve subpixel shifts in foil location, resulting in precision in axial strain measurement of 10^{-5} to 10^{-4} (Hansen et al., 2019).

Deformation experiments were conducted at temperatures and mean stresses of 800–1270°C and 1.6–9.7 GPa, respectively. Prior to deformation, each sample was annealed at temperatures of 800–1100°C for 5–20 minutes to relax any internal stress heterogeneity introduced during pressurisation (see Figure 1 of Wallis et al., 2020). To test which portion of the stress history the subgrain size records, all except one experiment were subjected to either steps in temperature, steps in strain rate, or both. At the end of each experiment, samples were quenched, the vertical anvils were withdrawn, and mean stress from the main loading ram was decreased slowly under approximately hydrostatic conditions.

2.4 Microstructural Analysis

To prepare the samples for microstructural analysis after deformation, the graphite furnace and all components within were extracted from the sample assembly and mounted on a glass slide using Logitech Epothin resin. Thick sections were formed by grinding the experimental column down on a Buehler Petrothin, at the University of Oxford, until it was a thickness of 1.2–1.8 mm. The ground surface was subsequently remounted on a fresh glass slide, the old glass slide removed, and the new free surface ground until a central section of the sample remained. At this stage, blobs of UV resin were placed around the

edges of the slides to help stabilise the samples during final polishing. Samples were then reground on the Petrothin to thicknesses in the range 0.2–0.6 mm with a flat central section exposed for polishing. All surfaces were polished with a Planocloth polishing cloth, 0.3 µm alumina powder, and water for 2–4 hours. Samples were subsequently polished with colloidal silica, as necessary, for 0.3–2.5 hours. Prior to EBSD data collection, samples were coated with 5–8 nm of carbon to minimise charging in the scanning electron microscope.

EBSD data were collected on a field-emission gun scanning-electron microscope (FEG-SEM) either at the Department of Earth Sciences, University of Oxford; the Marine Biological Laboratory (Woods Hole); or the Characterization Facility, University of Minnesota. At the University of Oxford, data were collected on an FEI Quanta 650 E-SEM equipped with Oxford Instruments AZtec acquisition software and a NordlysNano EBSD camera. At the Marine Biological Laboratory, data were collected using a Zeiss Supra 40VP FEG-SEM equipped with an Oxford Instruments Symmetry EBSD detector. At the University of Minnesota, EBSD data were collected using a JEOL 6500 FEG-SEM with an Oxford Instruments Symmetry S2 EBSD detector. In all three systems, samples were tilted to 70° and mapped at either low-vacuum (50–70 Pa H_2O or N_2) or high-vacuum conditions, at an accelerating voltage of 20–30 kV, with a step size of 0.075–0.5 µm. Collection conditions for individual samples can be found in Supplementary Table S1.

Data were processed using a combination of Oxford Instruments' Channel5 or AZtecCrystal software and the MTEX toolbox (version 5.7) for MATLAB® (Bachmann et al., 2010). First, spurious olivine pixels with systematic misindexing due to pseudosymmetry were corrected by applying a rotation of 60° around $[100]$ (Bystricky et al., 2006) in Channel5 or AZtecCrystal. EBSD data were then processed with the MTEX toolbox. Isolated pixels and "grains" comprised of < 3 pixels were removed. Pixels with mean angular deviation (MAD) values $> 1°$ were also removed. Subsequently, all non-indexed pixels, which comprise 2–38% (average 21%) of each map, were filled in MTEX using a nearest-neighbour method, whereby empty pixels are assigned the phase and orientation of the nearest indexed pixel. Interpolation was required for subgrain-size analysis as the centre of non-indexed regions are set to be boundaries in the current line-intercept MATLAB script, and could therefore result in inaccurate stress estimates. Figure S1 in the supplementary information presents phase maps of EBSD data prior to the infill of non-indexed regions.

To test the effect of indexing rate on the piezometric stress measurements, samples were further polished with colloidal silica and new maps were collected for the olivine-orthopyroxenite sample in San502 and for both the olivine stress sensor and harzburgite samples in San508, two key samples where the original maps contained high proportions of non-indexed pixels (25–40%). Despite the indexing rate being increased by up to 27%, the change in estimated stress was generally negligible (between 0–15%), and has no effect on the overall conclusions of this work.

2.5 Subgrain-size Piezometry

We conducted subgrain size piezometry following the procedures laid out by Goddard et al. (2020). Goddard et al. (2020) presented a single subgrain-size piezometer calibrated from EBSD maps of deformed quartz aggregates and olivine aggregates, in which subgrain size was normalised by the Burgers vector, and differential stress was normalised by the shear modulus. Subgrain size was defined as the average spacing between boundaries with misorientation angles $\geq 1°$. As such, it is important to ensure that EBSD maps have angular precision $< 1°$ (ideally $< 0.5°$) to avoid the creation of spurious 1° boundaries. Here, we find that some EBSD maps contain isolated pixels misoriented from their neighbours by $\geq 1°$ (e.g., Supplementary Figure S2), which we attribute to two sources. First, angular uncertainties arising from application of the Hough transform for automated indexing, commonly on the order of 0.5° (Maitland & Sitzman, 2007). Second, high concentrations of isolated geometrically necessary dislocations, not contained within subgrain boundaries, given the relatively high differential stresses (> 1 GPa) experienced by samples in this study.

To avoid the inclusion of spurious 1° boundaries, we instead use a modified subgrain-size piezometer (Figure 3), recalculated for a critical misorientation angle of 2° from the EBSD maps used in the original calibration by Goddard et al. (2020) :

$$\frac{\lambda}{b} = 10^{1.1\pm0.3} \left(\frac{\sigma}{\mu}\right)^{-1.1\pm0.1} \tag{5}$$

where λ is the mean line-intercept length, b, is the Burgers vector, σ, is the equivalent stress, and μ is the shear modulus. This new calibration also includes an additional cleaning step of removing pixels with mean angular deviation of $> 1°$. Note that the stresses applied

to quartz in Figure 3 have also been corrected for friction in accordance with Holyoke and Kronenberg (2010).

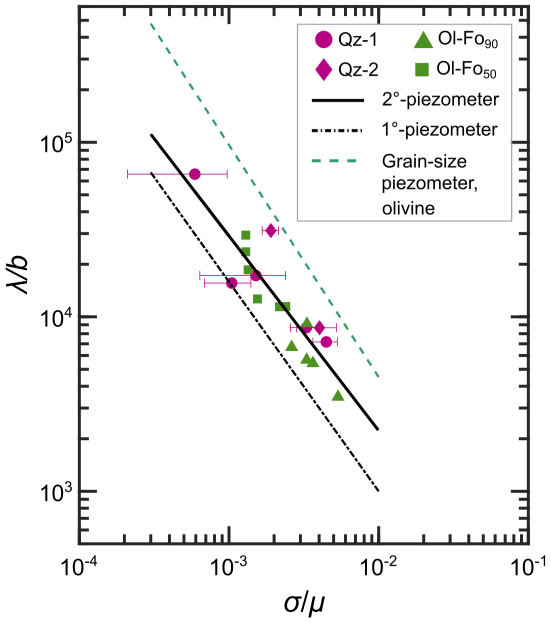

Figure 3. Recalibration of the subgrain-size piezometer based on boundaries with misorientation angles of $\geq 2°$. Mean line-intercept length, λ, normalised by the Burgers vector, b, is plotted as a function of the equivalent stress, σ, normalised by the shear modulus, μ. The original 1°-piezometer by Goddard et al. (2020) has been added for comparison (dashed black line) as well as the grain-size piezometer for olivine (van der Wal et al., 1993). Currently, no equivalent grain-size piezometer exists for orthopyroxene. For further explanation of the different data subsets, see Goddard et al. (2020).

For consistency with Goddard et al. (2020), subgrain size was measured using the line-intercept method. To ensure that we used an adequate number of intercepts for robust measurement of the subgrain size, we systematically increased the number of intercepts until the line-intercept length became essentially invariant (varying $< 2.5\%$ from the previous measurement). The mean-line intercept length was calculated as the arithmetic mean of intercepts measured both parallel and perpendicular to σ_1. The mean grain size of each phase, λ_{gs}, was also measured using the line-intercept method with the minimum misorientation angle of a grain boundary defined as 15°, and with no geometric correction applied.

For the initial calibration of the subgrain-size piezometer, temperature and pressure had a negligible impact on the shear modulus and Burgers vector values used to normalise

the piezometer, at least over the range of temperature-pressure conditions used in the calibration experiments (Goddard et al., 2020). However, the olivine samples used for the original piezometer calibration were deformed at a pressure of 0.3 GPa, which is significantly lower than the mean stresses used here (1.6–9.7 GPa). These elevated mean stresses have a particularly significant impact on the shear modulus of olivine, which increases by 4–16% relative to its value at room pressure. Therefore, we chose to correct the shear moduli and Burgers vectors of olivine and orthopyroxene using the pressure derivatives given in Table 1. The corrected Burgers vectors and shear moduli give stresses that, on average, are 7% greater than those based on using the uncorrected values, with a maximum difference of 12%.

For each piezometric stress estimate, an error was calculated using a Monte-Carlo-based approach. We assumed that the probability distribution of the subgrain size, pre-exponential constant, and exponent all follow lognormal distributions with standard deviations (in log units) of 0.13, 0.3, and 0.1, respectively, and with means given by the measured or best-fit values. These standard deviations were determined in the initial calibration of the subgrain piezometer, as described in Appendix A. We then randomly drew values from these distributions and used them to predict the differential stress. This process was repeated 10,000 times, and the standard deviation in the distribution of differential stresses was taken to be the error in the stress measurement. A full description of this method can be found in Appendix A.

Table 1. Pressure dependence of shear moduli and Burgers vectors for olivine and orthopyroxene

Mineral	G_o (GPa)	$\partial G/\partial P$	$\partial^2 G/\partial^2 P$ (GPa^{-1})		b (μm)	$\partial b/\partial P$ (μmGPa^{-1})	$\partial^2 b/\partial^2 P$ (μmGPa^{-2})
Ol	77.8[a]	1.71[b]	-0.054[b]	<a>	4.75[c] $\times 10^{-4}$	-8.377[b] $\times 10^{-3}$	2.088[b] $\times 10^{-4}$
Opx	78.1[d]	1.45[d]	0	<c>	5.20[e] $\times 10^{-4}$	-1.548[f] $\times 10^{-6}$	8.2180[f] $\times 10^{-8}$

[a] Mao et al. (2015)
[b] Abramson et al. (1997)
[c] Deer et al. (1988, page 4)
[d] Chai et al. (1997)
[e] Deer et al. (1988, page 158)
[f] Angel and Hugh-Jones (1994)

3 Results

3.1 Mechanical Data

We performed seven experiments in total: one with an olivine stress sensor stacked in series with an olivine-orthopyroxenite sample, five with an olivine stress sensor stacked in series with a harzburgite sample, and one with two samples of harzburgite stacked in series. Table 2 lists the temperatures, strain rates, mean stresses, and final strains for each sample. The final stress indicated by each diffraction peak can be found in Table 3, and the peak and average stresses can be found in Supplementary Tables S2 and S3, respectively.

3.1.1 Olivine Stress Sensor Stacked Against Olivine-Orthopyroxenite

Mechanical data for San502, which consisted of an olivine-orthopyroxenite sample stacked against an olivine stress sensor, are displayed in Figure 4. Due to the low proportion of olivine (15%) within the olivine-orthopyroxenite sample, stresses were only calculated for orthopyroxene. Initially, differential stress increased with strain. The apparent Young's modulus of ∼40 GPa from this period is too low to represent purely elastic deformation, which is associated with an elastic modulus of ∼200 GPa for olivine. As we measure stresses from the sample directly, we can rule out machine-compliance effects. Therefore, we infer that our experiments yielded early during loading and progressively hardened.

Samples were first deformed at a temperature of 800°C and at strain rates of 2.9×10^{-5} s^{-1} and 2.5×10^{-5} s^{-1}, for the olivine stress sensor and olivine-orthopyroxenite sample, respectively until a strain of 0.016 was reached in the olivine and a strain of 0.014 in the olivine orthopyroxenite. At this point, the displacement rate was decreased resulting in strain rates of 1.9×10^{-5} s^{-1} in the olivine and 1.4×10^{-5} s^{-1} in the olivine orthopyroxenite. After a further ∼0.02 strain, temperature was increased to 900°C so that deformation could continue at a lower differential stress. After the change in temperature, the olivine stress sensor and olivine-orthopyroxenite sample deformed at strain rates of 4.4×10^{-5} s^{-1} and 2.3×10^{-5} s^{-1}, respectively.

During the final deformation step, the average flow stresses in the olivine stress sensor (590–690 MPa) were similar to those measured from the {421} and {321} peaks in orthopyroxene within the olivine-orthopyroxenite sample (620 MPa and 670 MPa, respectively).

However, stresses measured from the {610} peak in orthopyroxene were considerably greater, averaging 1050 MPa.

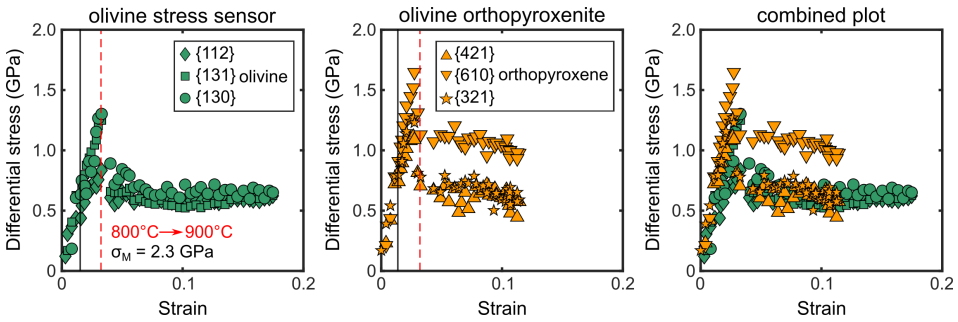

Figure 4. Stress as a function of strain for experiment San502, which consists of an olivine stress sensor paired against an olivine orthopyroxenite. Stresses from olivine and orthopyroxene are in green and orange, respectively. The red dashed vertical line represents a change in temperature, the black vertical line represents a change in displacement rate, and σ_{M} refers to the mean stress during the final conditions of the experiment (see Table 2 for values).

3.1.2 Olivine Stress Sensor Stacked Against Harzburgite

Mechanical data for the five experiments consisting of a harzburgite sample and olivine stress sensor are presented as stress-strain curves in Figure 5. Four of these experiments were deformed at temperatures in the range 1100–1270°C and average mean stresses in the range 4.7–9.4 GPa. Experiment San508 was deformed at 900°C and at average mean stresses of 1.6–2.5 GPa.

In all samples except the stress sensors in San391 and San404, stress initially increased with strain. Low apparent moduli from these portions of the stress-strain curves suggest that yielding was instantaneous within the temporal resolution of our experimental measurements. Steeper gradients at $< 1\%$ strain in the mixtures in San390 and San404 suggest deformation may have initially been elastic, but data from these segments of loading are sparse.

In most experiments, temperature and/or the displacement rate of the vertical rams were modified during deformation to change the differential stress. During experiments San391 and San396, the temperature was raised to decrease the differential stress. In experiment San404, the displacement rate of the vertical rams was reduced, also to decrease the differential stress. In experiments San396 and San508, the ram displacement rate was

instead increased. These changes in displacement rate and temperature are indicated in Table 2, and the stress-strain curves are presented Figure 5 .

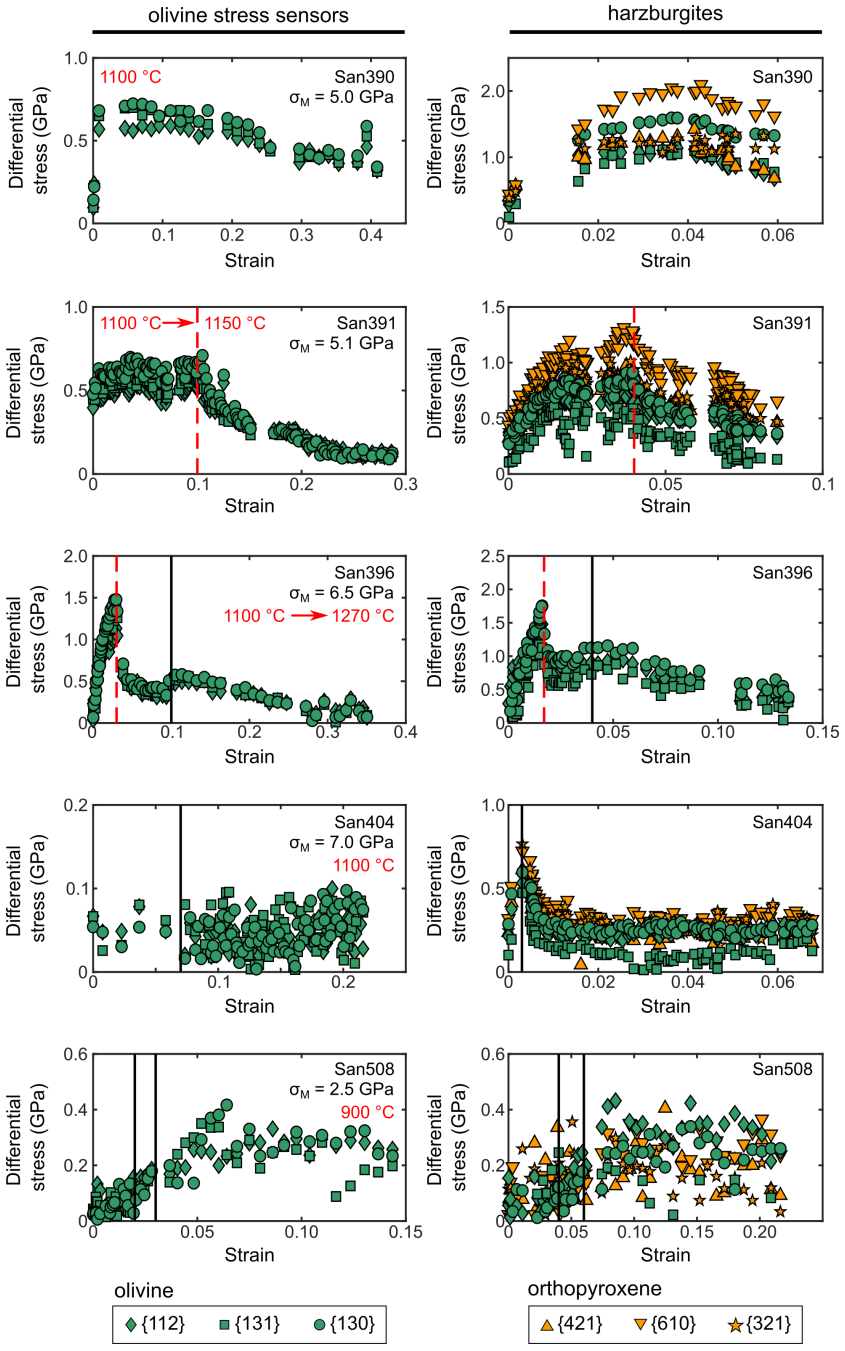

Figure 5. Stress as a function of strain for olivine stress sensors (left) paired against harzburgites (right). Stresses from olivine and orthopyroxene are in green and orange, respectively. The red dashed vertical lines represent changes in temperature, the black vertical lines represent changes in displacement rate, and σ_M refers to the mean stress during the final conditions of the experiment (see Table 2 for values).

Stresses in samples in San404 and San508 evolved to constant values whereas stresses in the other harzburgite-bearing experiments decreased progressively over time. This reduction in stress may be due to an increase in temperature as a result of changes to the furnace during deformation (e.g., changes in furnace shape or movement of the sample relative to the hot zone). As stated above, temperature is calculated based on a calibrated relationship between furnace power and temperature (Dixon & Durham, 2018). Therefore, deviations in the furnace shape or the position of a sample relative to the hot zone from that of the calibration assembly would lead to discrepancies between the calculated and actual temperature. As temperature is an input into the equation for mean stress (see Eqs 1 & 3), comparing the differential-stress and mean-stress curves can give an indication of whether temperature increased. An artificially low apparent temperature (i.e., when the temperature based on the furnace calibration is lower than the actual temperature experienced by the samples) leads to an artificially low apparent mean stress. Thus, a decrease in both mean stress and differential stress during an experiment may be indicative of an increase in temperature. The simultaneous drop in the calculated mean stresses (see Figure S3) and differential stresses suggests that temperature did increase throughout experiments San404 and San508. However, as mean stress and temperature only play a minor role in the calculation of the X-ray shear modulus and thus the calculation of the differential stress—and as piezometers are thought to be temperature independent (e.g., Stipp & Tullis, 2003)—the precise cause of the drop in stress is not directly relevant to this study.

In the olivine stress sensors, average stresses from each of the three diffraction peaks are typically consistent to within 20 MPa, with the exception of San390, which is consistent to within 70 MPa. For olivine within harzburgites, stresses from the three peaks differ by up to 450 MPa, with the {130} peak typically giving the greatest stress. For orthopyroxene in harzburgite, the difference in stresses calculated from the {421} and {321} peaks is within 40 MPa, with the exception of San390, where calculated stresses differ by up to 110 MPa. If stresses from the {610} peak are included, the difference in the stress increases up to 690 MPa.

For four of the experiments involving harzburgite, strain in the olivine stress sensor (0.22–0.41) was significantly greater than that in the harzburgite (0.06–0.13), indicating that harzburgite was stronger than olivine at the high pressures (4.7–9.4 GPa) and temperatures (1100–1270°C) of these experiments. Stresses measured in the harzburgite sample by X-ray diffraction were also, in all cases, greater in orthopyroxene than in olivine. In exper-

iment San396, the diffraction patterns in orthopyroxene in the harzburgite were too noisy to measure stress, and as such, it was not possible in this instance to compare how stress was partitioned between olivine and orthopyroxene.

In experiment San508, which was conducted at relatively low mean stresses of 1.6–2.5 GPa and a temperature of 900°C, strain was greater in the mixture (0.22) than in the olivine sample (0.16). Within the mixture, the average stresses calculated from the peaks from orthopyroxene (170–280 MPa) lay within the range of stresses calculated from the peaks from olivine (-50–330 MPa).

3.1.3 Harzburgite Stacked Against Harzburgite

To attain greater strains within harzburgite, two samples of the same composition were deformed together in a single experiment (San409), reaching a total strain of 0.28 (Figure 6). The samples initially deformed elastically, following the elastic modulus of harzburgite (Christensen, 1966), to strains of 0.005–0.01, after which the samples yielded and proceeded to strain harden. To take the samples through a variety of different stresses, the temperature and displacement rate of the experiment were modified at four and three points, respectively (see Table 2 and Figure 6). Temperature was first increased from 1100°C to 1150°C, and then subsequently increased further to 1250°C. After $\sim$0.14 strain, the temperature was reduced to 1200°C and then further reduced to 1150°C at 0.23 strain to prevent the differential stress from relaxing below the noise level. Changes in the experimental conditions led to strain rates of 1.7×10^{-5} s^{-1} to 4.5×10^{-5} s^{-1}.

Average stresses calculated from the $\{421\}$ and $\{321\}$ peaks in orthopyroxene (290–410 MPa) are consistent with the stresses from the olivine peaks (180–430 MPa), whereas stresses calculated from the $\{610\}$ peaks were considerably greater (660 MPa and 690 MPa for the top and bottom samples, respectively).

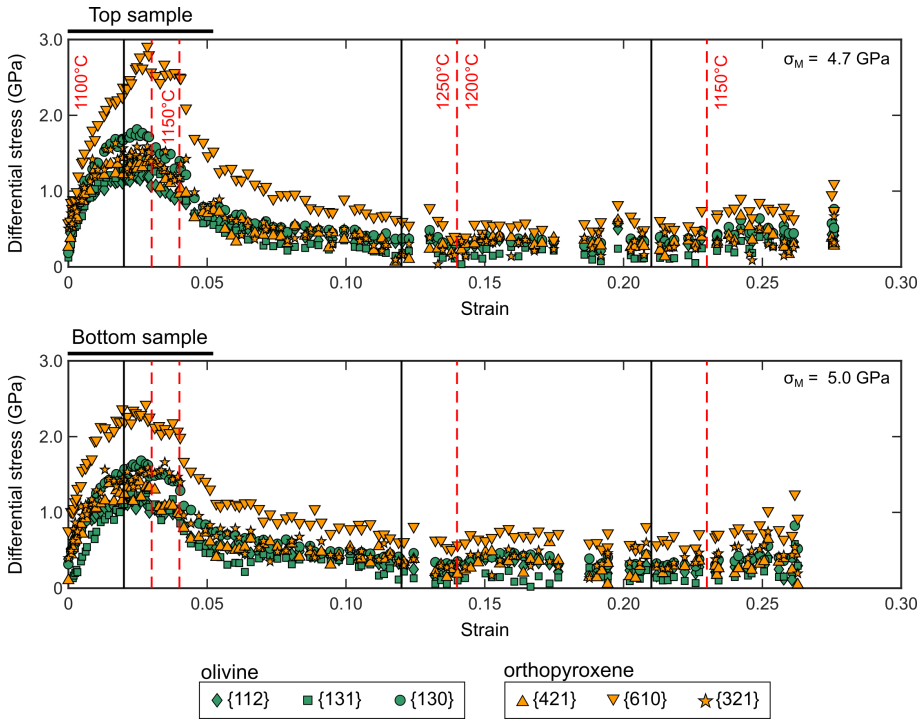

Figure 6. Stress versus strain curves for harzburgites in experiment San409. The central Ni foil was not usable for strain measurements in this experiment. As a result, stresses for each sample are plotted instead against the total strain of the combined sample stack. The red dashed vertical lines represent changes in temperature, the black vertical lines represent changes in displacement rate, and σ_{M} refers to the mean stress during the final conditions of the experiment (see Table 2 for values).

Table 2: Experimental Conditions

Experiment	Position	Sample	Starting material	Temperature (°C)	Strain rate[a] ($\times 10^{-5} s^{-1}$)	Average mean stress[b] (GPa)	Final mean stress (GPa)	Total strain
San390	Top	Ol	33	1100	22.3	5.0 ± 0.5	4.1	0.41
	Bottom	Hz(Px30)	PT-1299HiFe	1100	2.5	4.9 ± 0.5	4.1	0.06
San391	Top	Hz(Px30)	Pt-1299HiFe	1100	0.7	5.1 ± 0.2	5.5	0.04
				1150	0.2	5.0 ± 0.3	4.5	0.08
	Bottom	Ol	33	1100	1.8	5.2 ± 0.2	5.6	0.10
				1150	2.7	5.1 ± 0.3	4.6	0.28
San396	Top	Hz(Px30)	PL-1299HiFe	1100	1.3	9.1 ± 0.1	9.1	0.02
				1270	2.3	8.2 ± 0.3	7.8	0.04
				1270	9.0	6.3 ± 0.9	5.2	0.13
	Bottom	Ol	PT-1166	1100	2.3	9.4 ± 0.2	9.7	0.03
				1270	7.9	8.3 ± 0.3	7.9	0.10
				1270	22.0	6.5 ± 0.9	5.2	0.35
San404	Top	Ol	LT-DrySC	1100	8.6	7.2 ± 0.1	7.3	0.07
				1100	1.3	7.0 ± 0.1	6.9	0.22
	Bottom	Hz(Px30)	PL-1299HiFe	1100	0.7	7.0 ± 0.1	7.1	<0.01
				1100	0.6	7.0 ± 0.0	6.9	0.07
San409[c]	Top	Hz(Px30)	PL-1299HiFe	1100	1.7	7.7 ± 0.2	8.0	0.02
				1100	1.8	7.9 ± 0.0	8.0	0.03
				1150	1.8	7.7 ± 0.2	7.6	0.04
				1250	3.9	6.9 ± 0.4	6.3	0.12
				1250	4.5	6.0 ± 0.1	6.0	0.14
				1200	4.5	5.5 ± 0.3	4.9	0.21
				1200	4.2	4.9 ± 0.0	4.9	0.23
				1150	4.2	4.7 ± 0.2	5.0	0.28

Table 2 – continued from previous page

Experiment	Position	Sample	Starting material	Temperature (°C)	Strain rate[a] ($\times 10^{-5} s^{-1}$)	Average Mean stress[b] (GPa)	Final Mean stress (GPa)	Total strain
San409[c]	Bottom	Hz(Px30)	PL-1299-HiFe	1100	1.7	7.8 ± 0.2	8.1	0.02
				1100	1.8	8.1 ± 0.1	8.2	0.03
				1150	1.8	7.9 ± 0.1	7.8	0.04
				1250	3.9	7.0 ± 0.4	6.3	0.12
				1250	4.5	6.1 ± 0.1	6.0	0.14
				1200	4.5	5.6 ± 0.3	5.2	0.21
				1200	4.2	5.1 ± 0.1	5.1	0.23
				1150	4.2	5.0 ± 0.3	5.7	0.28
San502	Top	OrthoPy(Px85)	PI-2056	800	2.5	N/A	N/A	0.01
				800	1.4	N/A	N/A	0.03
				900	2.4	N/A	N/A	0.11
	Bottom	Ol	PI-2056-ol	800	2.9	2.5 ± 0.5	3.0	0.02
				800	1.9	3.2 ± 0.1	3.4	0.03
				900	4.4	2.3 ± 0.2	2.1	0.17
San508	Top	Hz(Px50)	PI-2056	900	3.3	1.6 ± 0.3	1.9	0.04
				900	3.6	2.1 ± 0.1	2.2	0.06
				900	5.6	2.5 ± 0.1	2.3	0.22
	Bottom	Ol	PI-2056-ol	900	1.2	2.0 ± 0.1	2.2	0.02
				900	2.3	2.3 ± 0.1	2.2	0.03
				900	4.8	2.5 ± 0.1	2.3	0.16

[a]Strain rate is taken as the gradient between strain and time fit through linear regression.
[b]Mean stress calculated using the {130} peak in the olivine in each sample.
[c]Due to a tilt in the middle foil, all reported strains and strain rates for this experiment are the average for the entire assembly.

Table 3. Final stresses measured by X-ray diffraction, rounded to the nearest 10 MPa.

Experiment	Sample[a]	Final stress: X-ray diffraction (MPa)					
		Olivine			Orthopyroxene		
		{112}	{131}	{130}	{421}	{610}	{321}
San390	OSS	320	310	340	-	-	-
	Mix	680	780	1330	680	1620	1130
San391	OSS	110	120	90	-	-	-
	Mix	350	140	390	380	590	500
San396	OSS	70	90	70	-	-	-
	Mix	330	310	390	-	-	-
San404	OSS	30	70	70	-	-	-
	Mix	260	130	280	170	310	220
San409	Mix:Top	420	320	510	310	740	320
	Mix:Bot	300	300	520	50	920	190
San502	OSS	620	630	650	-	-	-
	Mix	-	-	-	440	930	580
San508	OSS	230	220	180	-	-	-
	Mix	250	-60	260	90	240	30

[a]OSS: Olivine stress sensor, Mix: Harzburgite or olivine orthopyroxenite

3.2 Microstructural Analysis

A map of kernel-average misorientation (KAM) for each sample is presented in Figure 7. Subgrain boundaries are common in olivine, both in the stress sensors and mixtures, and particularly in samples deformed at temperatures $\geq$ 1100°C. In orthopyroxene, subgrain boundaries are sparse (if present at all) in experiments conducted at high temperatures and mean stresses, with the exception of experiment San409, in which the stacked harzburgites reached a strain of 0.28 (Figure 6). However, subgrain boundaries are pervasive within orthopyroxene in the experiments conducted at lower temperatures and mean stresses (San502 and San508).

Average intercept lengths for boundaries with a misorientation angle of $\geq 15°$ (i.e., grain boundaries) in the olivine stress sensors range from 1.6–6.6 µm. In the mixtures, the mean lengths are 1.9–3.7 µm and 1.7–3.0 µm for olivine and orthopyroxene, respectively. Where possible, comparisons to the initial starting microstructures show that grains within the olivine stress sensors are ~30% smaller after deformation, whereas within the mixtures

the grain size remains roughly constant. Mean line-intercept lengths between boundaries with a misorientation angle of $\geq 2°$ (i.e., subgrain boundaries and grain boundaries) are 1.3–4.8 µm in the olivine stress sensors, corresponding to stresses of 190–630 MPa as estimated by the subgrain-size piezometer (Eq. 5). In the mixtures, mean line-intercept lengths for olivine (1.2–2.9 µm) and orthopyroxene (1.5–2.7 µm) correspond to estimated stresses of 300–680 MPa and 340–590 MPa, respectively. The average boundary spacing and the associated stresses are presented in Table 4.

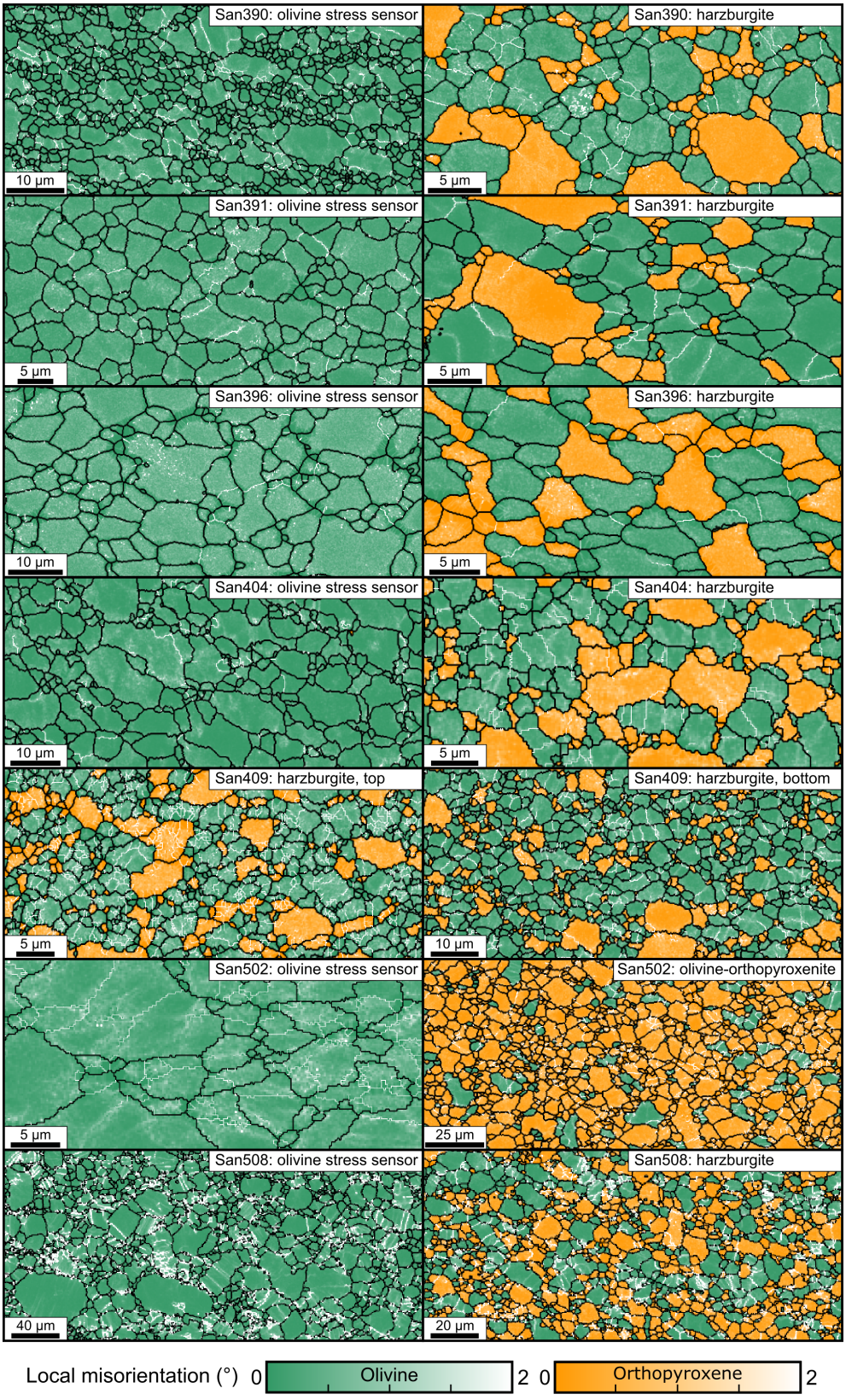

Figure 7. Subsets of local misorientation maps from EBSD data. Phase maps of the full, unfilled datasets are presented in Figure S1 in the supplementary information. Grain and subgrain boundaries are displayed in black and white, respectively and are defined as boundaries with misorientation angles of $\geq 15°$ and $\geq 2°$. The compressional axis is vertical.

Table 4. Grain-size measurement (λ_{gs}) and subgrain boundary spacing, that is subgrain size, measurement (λ) with associated piezometric stresses and errors. Both (λ_{gs}) and (λ) were measured using the mean-line intercept method.

Experiment	Position	Index	Average	Grain-size measurement			Subgrain-size measurement			
		rate (%)	MAD (°)	Phase	No. Intercepts	λ_{gs} (μm)	No.intercepts	λ (μm)	Stress (MPa)	Error (MPa)
San390	Top	72	0.40±0.33	Ol	60	1.6	60	1.3	630	+820/-360
	Bottom	68	0.51±0.38	Ol	60	1.9	60	1.5	550	+720/-310
				Opx	50	1.7	60	1.5	590	+760/-340
San391	Top	87	0.37±0.26	Ol	60	2.2	70	1.9	450	+610/-260
				Opx	90	2.1	90	2.0	460	+620/-260
	Bottom	86	0.45±0.30	Ol	70	2.6	70	2.3	380	+510/-220
San396	Top	62	0.41±0.36	Ol	40	2.3	70	2.2	400	+530/-230
				Opx	80	2.8	70	2.5	370	+520/-210
	Bottom	69	0.51±0.38	Ol	70	3.7	70	3.2	290	+400/-170
San404	Top	91	0.33±0.30	Ol	40	3.0	60	2.8	330	+460/-190
	Bottom	83	0.44±0.36	Ol	30	2.0	70	1.6	550	+720/-300
				Opx	70	2.0	70	1.8	520	+700/-300
San409	Top	65	0.63±0.53	Ol	60	1.9	60	1.2	680	+890/-380
				Opx	80	2.3	80	1.5	600	+780/-340
	Bottom	82	0.50±0.38	Ol	60	1.9	60	1.5	570	+750/-320
				Opx	60	1.8	80	1.6	580	+750/-330
San502	Top	79	0.45±0.35	Ol	80	3.0	80	2.3	370	+490/-210
				Opx	60	3.0	70	2.7	340	+460/-200
	Bottom	80	0.51±0.36	Ol	60	4.0	70	2.1	390 480[a]	+520/-230 +760/-300
San508	Top	87	0.39±0.32	Ol	80	3.7	80	2.9	300	+410/-180
				Opx	80	2.7	60	2.4	380	+510/-220
	Bottom	98	0.29±0.21	Ol	60	6.6	80	4.8	190	+270/-110

[a]Calculated using the [001] Burger's vector for olivine, see Appendix B

manuscript submitted to *JGR: Solid Earth*

4 Discussion

4.1 Comparing *In-situ* and *Ex-situ* Stress Measurements

A more complete understanding of the tectonic processes that occur on Earth requires constraints on the strength of the lower crust and mantle, both of which are generally made up of more than one mineral. The recent calibration of an EBSD-based subgrain-size piezometer (Goddard et al., 2020) offers new opportunities for estimating paleostress magnitudes within exhumed polymineralic rocks, while avoiding the potential effects of grain-boundary pinning by secondary phases. However, to date, no study has tested whether subgrain size accurately reflects stresses supported by individual phases within polymineralic rocks, nor what these piezometric stresses tell us about the overall stress experienced by an aggregate. In this study, we present the first direct comparison of stresses measured *in-situ* within individual phases to those recorded by the subgrain-size piezometer.

For consistency with the piezometer of Goddard et al. (2020), we begin by considering the final *in-situ* stress experienced by each sample. While we have a single stress to consider from subgrain-size piezometry, the different diffraction peaks in both olivine and orthopyroxene provide a range of stresses. This variation in stress is a result of the plastic anisotropy of olivine and orthopyroxene, as grains within plastically anisotropic materials subjected to a non-hydrostatic stress field will undergo different amounts of plastic strain depending on their orientation (e.g., Ashby, 1970). This heterogeneity in plastic strain is accompanied by heterogeneity in elastic strain. As such, grains in different orientations experience different stresses (Karato, 2021; Li et al., 2006; Wang et al., 2003; Weidner et al., 2010). Here, we find that the {130} peak from olivine resulted in stresses on average 1.5 times greater than those from the other olivine peaks, consistent with previous observations (e.g., Weidner et al., 2010). For orthopyroxene, the {610} peak resulted in the greatest stress, on average 1.6 times greater than the {421} and {321} peaks. Previous studies have taken the average of the stresses measured from individual diffraction peaks to represent the macroscopic differential stress experienced by the sample (e.g., Li et al., 2006). However, it is unclear whether or not the stresses measured from different diffraction peaks should be evenly weighted (c.f., Burnley & Kaboli, 2019). Instead, the comparison of piezometric stresses from a single phase to those estimated from different diffraction peaks may shed light on which peaks best represent the macroscopic stress in our experiments.

Before comparing these *in-situ* stress measurements to those gathered *ex-situ*, it is first important to ensure that sufficient substructure developed for subgrain-size piezometry, a criterion not met by all the samples in this study (e.g., the olivine stress sensors of San396 and San404, Figure 7). One possible explanation for the lack of substructure is that the grains in these samples are too small to contain subgrains of the size predicted by the subgrain-size piezometer. For example, extrapolation of the grain- and subgrain-size piezometers of Twiss (1977) to greater stresses results in a theoretical subgrain size larger than the steady-state grain size. To test whether the grain size in our samples was large enough for subgrains to form, we calculated the predicted mean-line intercept length between subgrain boundaries, herein referred to as subgrain size, using the final stress measured from each X-ray peak and the pressure-corrected Burgers vectors and shear moduli. For each mineral, the predicted subgrain size was then compared to the measured grain size to assess whether subgrains would be expected to form at the final stresses experienced by that sample. The predicted subgrain size and its comparison to grain size for each phase in each sample can be found in Table S4 of the supplementary information.

For the olivine stress sensors in San390, San391, San396, and San404, all predicted subgrain sizes exceed the measured grain size. Similarly, the predicted subgrain sizes for both olivine and orthopyroxene in the harzburgite samples of San404 and in orthopyroxene in the harzburgite sample of San508 exceeded the measured grain sizes of the respective phases. Thus, subgrains were likely not able to form in a manner consistent with the subgrain-size piezometer, and consequently, we do not include these samples in our initial analysis.

For some samples, the range in stresses calculated from X-ray diffraction resulted in predicted subgrain sizes that straddled the measured grain size. Specifically, the stress measured from the {130} peak from olivine in the harzburgites of experiments San391, San396, San409, and San508, as well as the stress measured from the {112} peak in San508, are the only ones predicted to be sufficient to produce subgrains within the constraints of the grain size. Similarly, for orthopyroxene only the {610} and {321} peaks in San391 and the {610} peaks in San409 give stresses great enough to predict subgrain sizes smaller than the grain sizes. In our analysis, we include these samples but identify those diffraction peaks that give stresses too low for subgrain boundaries to be extensively developed at the measured grain sizes.

For olivine, stresses from subgrain-size piezometry are plotted against a range of stresses measured from X-ray diffraction in Figure 8. Open markers indicate individual diffraction peaks for which the stress was sufficiently low that the subgrain size predicted by the piezometer is larger than the grain size of the sample. Based on analysis of the activity of different slip systems (see Appendix B), a piezometric stress was also calculated for the olivine stress sensor of San502 by normalising the line-intercept length by the [001] Burgers vector (5.98Å, Deer et al., 1988, page 4, pressure correction from Abramson et al., 1997) rather than the [100] Burgers vector used for the other olivine samples. The change in Burgers vector increases the calculated stress from 390 to 480 MPa for San502. The stresses calculated using the [100] and the [001] Burgers vectors are both plotted in Figure 8 for comparison.

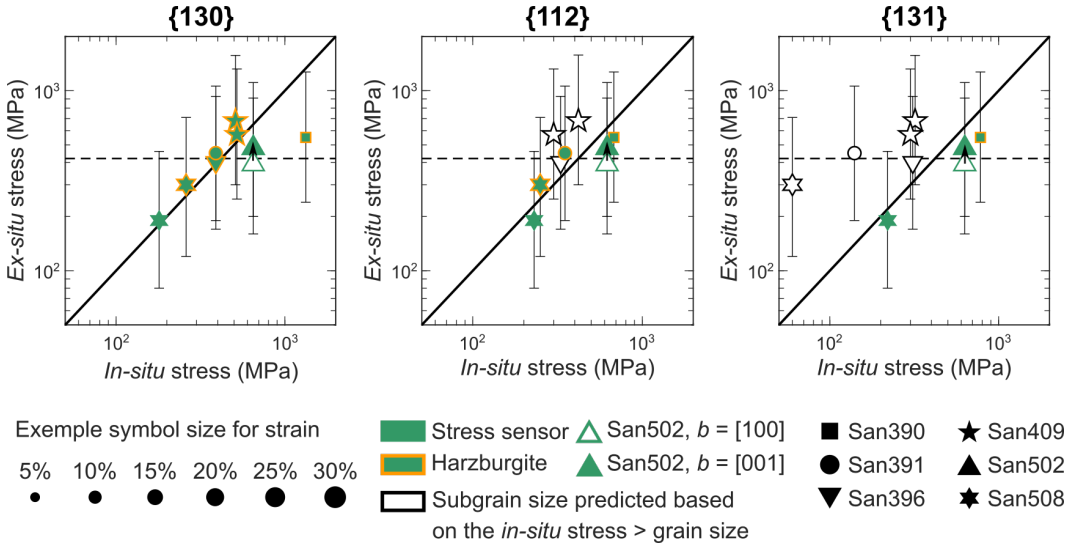

Figure 8. Comparison of *ex-situ* stresses from subgrain-size piezometry and final *in-situ* stresses from X-ray diffraction from olivine in both monomineralic and polymineralic samples. Error bars are calculated using a Monte-Carlo based approach, as described in Section 2.5 and Appendix A. The size of each data point is scaled by the total strain experienced by the sample. Stresses from individual X-ray peaks for which the predicted subgrain size is larger than the measured grain size of the sample are plotted as open symbols. The black solid line is 1:1 and the dashed horizontal line marks the upper calibration limit for olivine in the subgrain-size piezometer (Goddard et al., 2020). Two stresses from subgrain-size piezometry have been plotted for the stress sensor of San502, one where the mean-line intercept length was normalised by the length of the [100] Burgers vector and one where it was normalised by the length of the [001] Burgers vector.

A strong correlation exists between the *in-situ* stress measurements from the {130} diffraction peaks and the *ex-situ* stress measurements, in both the monomineralic and polymineralic samples (Figure 8). A moderate correlation also exists for the {112} peak, as these stresses are often similar to those from the {130} peak. The stresses from the {131} peak tend to be significantly lower than those calculated from the other diffraction peaks, and in most cases are low enough that the subgrain size predicted by the piezometer is larger than the measured grain size (open symbols in Figure 8). For the few samples that can confidently be compared, X-ray stresses from the {131} peak lie within the uncertainty of the piezometric stresses. Recently, Girard and Karato (2022) demonstrated that the bulk stress experienced by a sample is most accurately represented by the diffraction peak providing the greatest stress measurement, here the {130} olivine peak. Given the particularly close correspondence between the {130} stresses and the stresses measured via subgrain-size piezometry, we conclude that subgrain-size piezometry accurately reflects the stress within individual phases in a polymineralic rock.

Subgrain-size piezometry therefore provides a powerful tool for measuring stress in natural rocks, but care must be taken when applying it to extremely fine-grained samples. For example, olivine within polymineralic regions of the Erro-Tobbio peridotite in Italy, have average grain sizes as low as 5 µm (Linckens & Tholen, 2021). Such small grain sizes would require differential stresses of > 175 MPa to form subgrains, an unrealistic condition considering shear zones are regions of weakening and localisation (e.g., Skemer et al., 2010; Stenvall et al., 2019; Warren & Hirth, 2006). As many other natural shear zones, such as the Josephine peridotite (~ 250 µm, Hansen & Warren, 2015) and the Oman-United Arab Emirates ophiolite (≥ 100 µm Ambrose et al., 2018), are relatively coarse grained, the application of subgrain-size piezometry remains broad.

4.2 Subgrain-size Piezometry as a Tool For Unpicking Complex Stress Histories

A key challenge in paleopiezometry lies in accounting for the potentially complex stress histories experienced by natural samples, compared to samples deformed in the laboratory that often experience steady-state deformation (Kidder et al., 2016; Speciale et al., 2022). It is currently not clear how much strain is required to set or reset the stress recorded by the subgrain size. Previous work on olivine by Ross et al. (1980) compared constant strain rate and constant stress experiments to those in which the stress, strain rate, or temperature was varied incrementally. In those experiments, subgrain sizes were

found to decrease with increasing stress but did not coarsen with decreasing stress, suggesting that the subgrain size is set by the maximum stress applied to a sample. However, experiments on steel by Qin et al. (2003) found that subgrains were able to coarsen if continuously strained under stresses of a reduced magnitude, suggesting that strain, rather than time, is important for subgrain coarsening. Goddard et al. (2020) also demonstrated a correlation between subgrain-boundary spacing and the final stress experienced by olivine and quartz deformed in the laboratory, despite some samples having experienced greater (peak) stresses earlier in their deformation history.

To test how subgrain sizes respond to complex stress histories, we subjected the samples in all but one of our experiments to either temperature or strain-rate steps, which imparted strains between 0.01 and 0.25. Based on the initial calibration by Goddard et al. (2020), we would expect stresses estimated using the subgrain-size piezometer to match the final stresses measured through X-ray diffraction. Indeed, as seen in the previous section, such a correlation is apparent in Figure 8. However, some of the samples with grain sizes predicted to be too small to contain subgrains still contain numerous subgrain boundaries (e.g., the olivine stress sensor in San390 and the harzburgite in San404 in Figure 7). It is therefore possible that the subgrain boundaries within these samples formed during an earlier portion of the deformation history under a differential stress greater than the final stress.

To explore whether these 'unexpected' subgrain boundaries correspond to an earlier part of the deformation history, we plot in Figure 9 both the peak stresses and the final stresses measured by X-ray diffraction for samples not presented in Figure 8. To be clear, in all these remaining experiments the grain sizes were too small to accommodate subgrains of the size predicted by the piezometer based on the final stress measured by X-ray diffraction. We exclude data from the olivine stress sensor for experiment San404, as the predicted subgrain size from the peak stress was also too large to be accommodated within the grains.

The subgrain size in the samples with the most prolific intragranular boundaries give piezometric stresses that match the peak stress experienced during each experiment. The remaining two samples—the olivine stress sensors in experiments San391 and San396—give piezometric stresses that are midway through the peak stress and the final stress implying that their subgrains underwent some coarsening. Notably, during experiments San391 and

San396 the stress reductions were the result of increases in temperature from 1100°C to 1150°C and 1100°C to 1270°C, respectively. The two experiments that instead record the peak stresses were held at 1100°C. We therefore conclude that, at higher temperatures, subgrain boundaries are more easily removed. Ross et al. (1980) conducted experiments at temperatures of 1000–1300°C, however the majority of experiments used for piezometry were conducted at 1100°C. Our experiments at the equivalent temperature that exhibit little subgrain evolution are roughly consistent with the observations of Ross et al. (1980). Therefore, if the grain size is too fine for the subgrains to coarsen to the size determined by a new lower stress, and temperatures are relatively low, subgrain structure within a rock could relate to a previous, even transient, high stress.

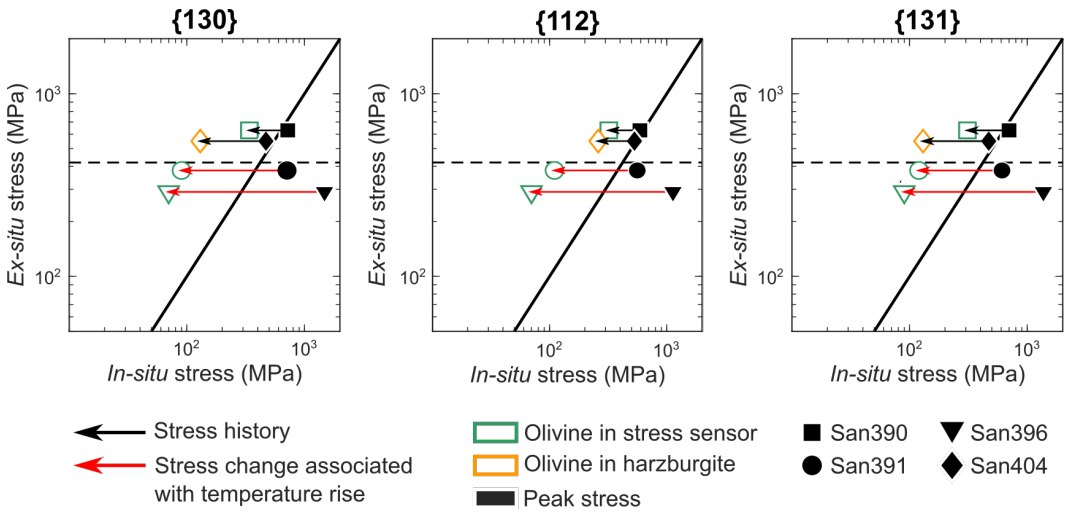

Figure 9. Comparison of *ex-situ* stress, from subgrain-size piezometry, and *in-situ* stress, from X-ray diffraction, for olivine in all samples for which the subgrain size predicted by the final stress was larger than the measured grain size. Black symbols represent the peak stress measured by X-ray diffraction. Horizontal arrows link the peak stress to the final stress experienced by the sample. The black solid line is 1:1 and the dashed horizontal line represents the calibration limit for olivine in the subgrain-size piezometer (Goddard et al., 2020). For clarity we did not include error bars, though errors on the piezometric stress estimates can be found in Table 4.

4.3 Subgrain-size Piezometry in Orthopyroxene

The experiments presented here provide an opportunity to explore whether the subgrain-size piezometer published by Goddard et al. (2020) can be reliably applied to orthopyroxene, a mineral not included in the original calibration. Such analysis would greatly expand the use of this piezometer and negate the common requirement to calibrate a subgrain-size piezometer for each mineral of interest. Stresses from subgrain-size piezometry of orthopy-

roxene are plotted against those from X-ray diffraction in Figure 10. Similar to Figures 8 and 9, we identify, with open symbols, stresses from X-ray diffraction that are too low for subgrains to form at the grain sizes of these samples.

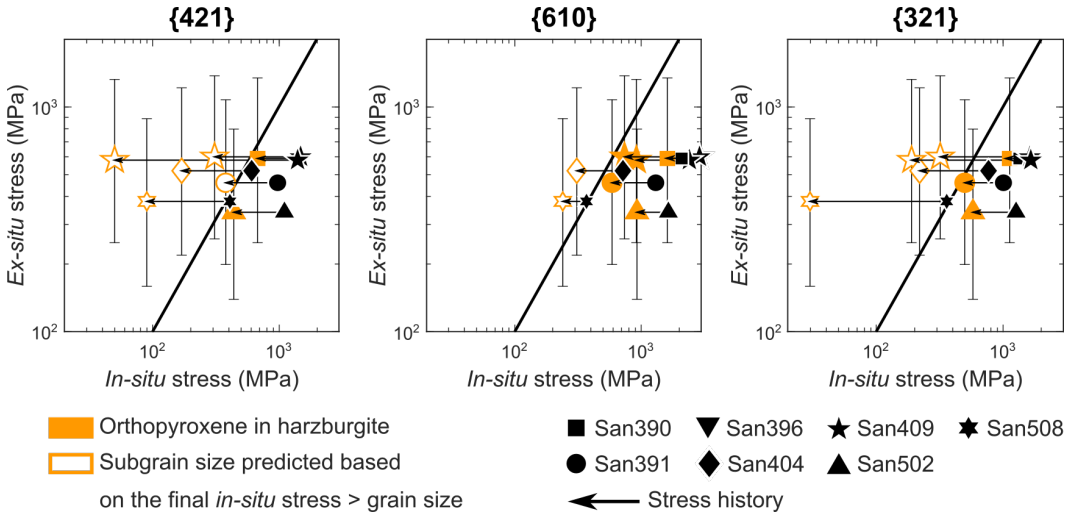

Figure 10. Comparison of *ex-situ* stress, from subgrain-size piezometry, and *in-situ* stress, from X-ray diffraction, for orthopyroxene in all samples. Black symbols represent the peak stress measured by X-ray diffraction and black horizontal arrows link the peak stress to the final stress experienced by the sample. Error bars are calculated using the Monte-Carlo based approach, as described in Section 2.5 and Appendix A. Stresses from individual peaks for which the subgrain size predicted by the piezometer was larger than the measured grain size are plotted as open symbols. The black solid line is 1:1.

There is no consistent relationship between the stresses preserved by the subgrain-boundary spacing in orthopyroxene and either the peak stresses or the final stresses experienced by the sample. However, this lack of correlation is expected given the limited intragranular substructure within the orthopyroxene in most samples. In addition, the low total strains in most of the mixtures, alongside the greater strength of orthopyroxene compared to olivine at high confining pressures (e.g., Raterron et al., 2016), indicates that the former may account for very little of the total strain of the aggregate. We therefore limit further discussion to experiments San409 and San508, in which the total strain of the harzburgite exceeds 0.20, and experiment San502, in which the sample is mostly orthopyroxene (85%) and a total strain of 0.11 was reached.

For experiment San409, the final stresses in the top and bottom samples measured through X-ray diffraction (310–740 MPa and 50–920 MPa, respectively) straddle those measured by subgrain-size piezometry (600 MPa and 580 MPa, respectively), though the large

range in *in-situ* stresses limits the significance of this comparison. For experiment San502, the stress of 340 MPa from subgrain-size piezometry is close to the final stress of 440 MPa measured from the {421} peak, but is less than the stresses of 930 MPa and 580 MPa from the {610} and {321} diffraction peaks, respectively. For San508, the grain size is too small to form subgrains of the size predicted by the piezometer based on the final stress. However, the stresses from X-ray diffraction only began to drop during the final 0.02 of strain. The previous 0.12 of strain occurred under a near constant stress of 360–410 MPa, which is consistent with the stress of 380 MPa measured in the orthopyroxene by subgrain-size piezometry.

These results broadly support the use of subgrain-size piezometry on orthopyroxene as long as sufficient substructure exists. These experiments also highlight the effects of large strength contrasts when applying the subgrain-size piezometer, as the strain experienced by an individual mineral is an important factor in determining whether subgrains in that mineral evolve to the size predicted by the piezometric relationship.

4.4 Stress Partitioning from X-ray Diffraction

The results of this study are, to the best of our knowledge, the first to provide direct evidence that subgrain sizes reflect the stress supported by an individual phase deforming in an aggregate. A relevant question that still remains, however, is how these measured stresses relate to the macroscopic stress applied to the rock. In the work presented here, the general lack of subgrains in orthopyroxene within experiments deformed at a high mean stress limits the use of subgrain-size piezometry as a tool for exploring stress partitioning. However, stress partitioning can still be explored via X-ray diffraction. Relatively few studies to date have used X-ray diffraction in this way (Li et al., 2007; Wang et al., 2013) and no studies, to our knowledge, have used this method in olivine-orthopyroxene systems.

When considering stress partitioning, the relevant question is how the stress within an individual phase relates to the bulk stress experienced by a rock. Stacked samples have previously been assumed to nominally experience the same stress (e.g., Hansen et al., 2019). This assumption holds true for our experiment San409, in which the same material was used for both the top and bottom samples (Figure 6). If the same were true of our other experiments, then the stress supported by the sample of monomineralic olivine in each ex-

periment should represent the bulk stress of the adjacent polymineralic sample. However, in all experiments conducted at high mean stresses ($>$ 5 GPa), differential stresses measured within the mixture were significantly greater than those in the olivine stress sensor (Figure 5). Silber et al. (2022) suggested that such differences in stress within an assembly can occur if the samples are weak relative to the confining medium. Our stacked samples cannot therefore be used to explore how stresses within each phase relate to the bulk stress, but we can see how different conditions affect the relative stresses within olivine and orthopyroxene.

We calculated the average stress from each peak over the final controlled conditions of the experiment, that is, after the final temperature or displacement-rate step (see supplementary Table S3). For experiment San409, we instead averaged stress over the final 0.2 strain, due to the small amount of strain under each set of conditions. Of the stresses calculated from the three peaks, we consider the least and greatest values to represent the 'stress range' of each phase in the mixture, and compare these in Figure 11. In experiments performed at high mean stresses ($>$ 5 GPa) and temperatures (1100–1270°C), the mean of three X-ray diffraction stresses is 1.2–1.7 times greater in orthopyroxene than olivine. However, in experiment San508, which was deformed at a lower mean stress of $\leq$ 4 GPa, the stresses supported by olivine and orthopyroxene are the same within error.

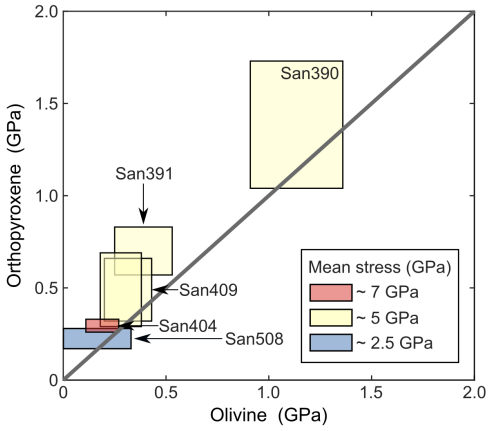

Figure 11. Comparison of the average differential stresses measured in olivine and orthopyroxene by X-ray diffraction. The boxes, colour coded for mean stress, cover the full range of stresses calculated from the different diffraction peaks of each phase.

This observation of a greater stress supported by the orthopyroxene when at high mean stress can be considered in relation to Handy's (1994) rheological mixing model.

As the harzburgites in this study consist mainly of olivine (∼70%), and as orthopyroxene is stronger than olivine at these experimental conditions (e.g., Raterron et al., 2016), the phase distribution within these samples can be categorised as interconnected weak layers (Handy, 1990). Stresses within the individual phases of samples with interconnected weak layers have been proposed to lie close to the isostress limit (Handy, 1994), also known as the Sachs model, in which it is assumed that each grain within an aggregate experiences the same stress tensor (Sachs, 1928). Handy's (1994) model predicts a slight variation from the Sachs model, with marginally greater stress within the 'strong' phase in mixtures when the viscosity contrast between phases is less than one order of magnitude. The greater stresses within the strong orthopyroxene in this study are therefore consistent with Handy's (1994) model. Similarly, work by Li et al. (2007) using X-ray diffraction to explore stresses within composites of varying proportions of MgO and spinel measured greater stresses within the strong phase when it comprised just 25% of the mixture. Clearly, *in-situ* stress measurements make a good dataset to examine polymineralic mixing models, which can then enable more accurate interpretations of stress estimates from natural samples.

5 Conclusions

We deformed olivine and olivine-orthopyroxene mixtures in a D-DIA apparatus at temperatures and mean stresses similar to mantle conditions. *In-situ* stress measurements from X-ray diffraction are compared to *ex-situ* measurements from subgrain-size piezometry. A good correlation between the *in-situ* and *ex-situ* stresses in olivine in both monomineralic and polymineralic aggregates demonstrates that subgrain size is unaffected by grain-boundary pinning by secondary minerals. Subgrain size also displays a good correlation with the final stress experienced by the sample, even in experiments with complex stress histories. However, this study identifies a number of important factors to consider when applying subgrain-size piezometry to natural rocks. First, in polymineralic rocks, caution must be taken in applying the subgrain-size piezometer to strong minerals that undergo little strain, such as those behaving as passive clasts within a deforming matrix. Second, while some initial data for orthopyroxene looks promising, further experiments are still required to confirm the applicability of the Goddard et al. (2020) piezometer to minerals other than quartz and olivine, with which it was calibrated. Third, very fine-grained rocks may not have grain sizes sufficiently large to host subgrains that have formed under low stresses. Therefore, in particularly fine-grained samples, the stresses measured from ex-

isting subgrains may not necessarily record the most recent stress state if the associated subgrain size was larger than the grain size, but may instead record earlier deformation associated with greater stresses and finer subgrain sizes. Finally, for the compositional ratios of samples deformed at high mean stresses of 4.7–9.4 GPa in this study, the stresses supported by orthopyroxene and olivine in harzburgites are not equal. As such, care must be taken when extrapolating the stress measured from an individual phase to the bulk stress experienced by the sample.

6 Data Availability Statement

Mechanical data from the Deformation-DIA experiments alongside EBSD data of recovered samples are avaliable from OSF via https://doi.org/10.17605/OSF.IO/UATJG (Goddard et al., 2023). Codes for processing EBSD data can be found at `https://github.com/RellieGoddard/SGPiezometry.git`.

Appendix A Error Estimation on the Subgrain-size Piezometer

We use a Monte-Carlo-based approach to estimate the errors in our subgrain-size measurements, the errors in parameters in the subgrain-size piezometer, and errors in stress estimates. The procedures described here are carried out in log units under the assumption, which is validated below, that errors in measurements of subgrain size are lognormally distributed. As an initial step, we refit the piezometer to the data determined using a threshold misorientation angle of 2°, above which boundaries are measured. For each measurement of subgrain size used in this refitting, we assume that the probability of measuring the true subgrain size is represented by a normal distribution (in log units) with standard deviation equal to the error in subgrain-size measurement. This error is justified below to be approximately 0.13 log units. We then randomly select a value from that distribution and perturb the measured subgrain size by that amount. This new data set of stresses and perturbed subgrain sizes is then used to determine the parameter values for the subgrain-size piezometer using a linear least-squares approach. This process is repeated 10,000 times, randomly generating new perturbed measurements on each iteration. The distributions of best-fit parameter values determined over all of these iterations are illustrated in Figures A1a and b. The means of these distributions are, within three significant digits, equivalent to the parameter values determined by a least-squares fit to the unperturbed data set. We

760 take the standard deviation of these distributions to reflect the error in estimation of the
761 piezometer parameters, resulting in a pre-exponential constant of 1.1±0.3 and an exponent
762 of -1.1±0.1.

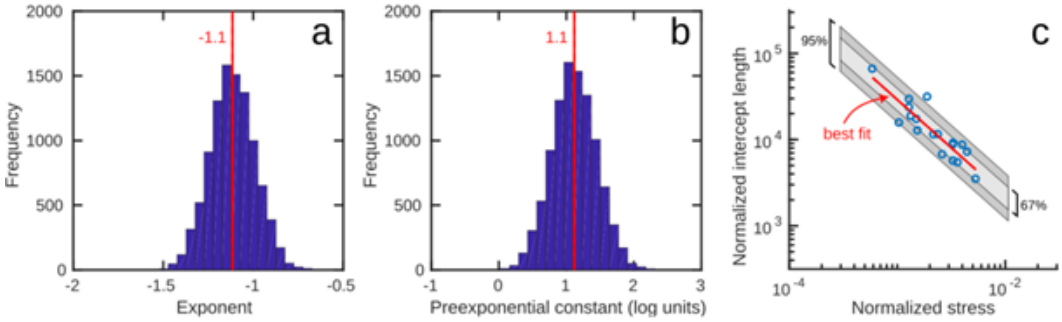

Figure A1. Estimation of error on best-fit parameters for the subgrain-size piezometer. Distributions of parameter estimates from 10,000 individual fitting exercises for (a) the exponent and (b) the preexponential constant in the piezometer. The means of the distributions are indicated in red. The standard deviations of the distributions are taken to represent the error in the estimate. (c) Best-fit piezometer compared to data used for calibration and 67% and 95% confidence intervals. Confidence intervals are estimated assuming that the error in subgrain-size measurement is 0.13 log units.

763 Figure A1 compares the best-fit piezometer to the measured data. This figure also
764 includes 67% and 95% confidence intervals determined using one or two times the error in
765 the subgrain-size measurement, respectively. We compare these confidence intervals to the
766 distribution of data as a check on the validity of our error estimation. We find that setting
767 the error on subgrain-size measurement to 0.13 log units, as presented in Figure A1, results
768 in 67% and 95% confidence intervals that contain 67% and 94% of the data, respectively.
769 This exercise not only demonstrates that an error of 0.13 log units in our subgrain-size
770 measurements is consistent with the data, but it also provides confidence that the error in
771 those measurements is lognormally distributed.

772 A similar procedure can be used to estimate the errors in stresses predicted using the
773 piezometer. Here we again assume that the probability distributions for the subgrain size,
774 pre-exponential constant, and exponent follow lognormal distributions with standard de-
775 viations (in log units) given by 0.13, 0.3, and 0.1, respectively, and with means given by the
776 measured or best-fit values. We randomly draw values from these distributions and use
777 them in conjunction with appropriate values of the Burgers vector and shear modulus to
778 make a prediction of the applied differential stress. This process is repeated 10,000 times to
779 generate a distribution of predicted stresses. The mean of this distribution (in log units) is

equivalent to the predicted stress used simply with the measured subgrain size and best-fit piezometer parameters. We take the standard deviation of this distribution to represent the error in the predicted stress. As an illustrative example, for a measured subgrain size of 1.5 µm with Burgers vector of 0.475 nm and shear modulus of 77.8 GPa, we estimate the normalised stress to be $10^{-2.2\pm0.4}$ and the absolute stress to be 510^{+680}_{-290} MPa.

Appendix B Choice of Burgers vector for Experiments San502 and San508

The subgrain-size piezometer presented by Goddard et al. (2020), was calibrated using high-temperature experiments in which dislocation creep of olivine occurs primarily by the slip system (010)[100] (e.g., Bai et al., 1991; Hansen et al., 2014; Wallis et al., 2019). However, two experiments from this study, San502 and San508, were carried out at lower temperatures ($\leq$ 900°C) where the (100)[001] slip system, and particularly [001] screw dislocations, can instead dominate deformation (e.g., Carter & Ave'Lallemant, 1970; Druiventak et al., 2011; Gaboriaud et al., 1981; Idrissi et al., 2016; Wallis et al., 2020). Here, we interpret the slip systems active in these two samples based on the pole figures and misorientation inverse pole figures. The pole figures are lower-hemisphere projections, are constructed using one point per grain and a kernel half-width of 5°, and are oriented such that the maximum principal stress axis (σ_1) is vertical. For all inverse pole figures, misorientation axes were plotted for neighbouring pixels with misorientation angles between 2° and 15°. Colour scales in Figures B1–B3 represent multiples of uniform distribution (MUD).

Pole figures and inverse pole figures for olivine in both the olivine stress sensor and the harzburgite sample of experiment San508 are plotted in Figure B1. Olivine exhibits a crystal preferred orientation (CPO) with [100] and [001] axes in girdles perpendicular to σ_1 and [010] axes in a cluster parallel to σ_1. Taken in isolation, this CPO indicates that (010) is the slip plane of the dominant slip system and that [100] and/or [001] is the dominant Burgers vector. The misorientation axes of olivine form a dominant cluster parallel to [001] and a secondary cluster parallel to [010]. Misorientation axes parallel to [001] are characteristic of tilt boundaries composed of edge dislocations on the (010)[100] slip system. Misorientation axes parallel to [010] can result from three possible types of subgrain boundary, specifically tilt boundaries composed of edge dislocations on the (001)[100] or (100)[001] slip systems and twist boundaries composed of [100] and [001] screw dislocations. Taken together, these observations indicate that (010)[100] was the dominant slip system, whilst (001)[100] and or (100)[001] were also active but to a lesser degree.

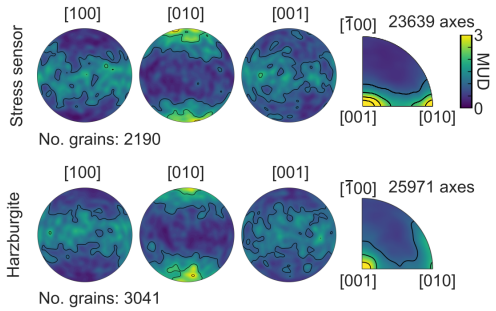

Figure B1. Pole and inverse pole figures for olivine in the stress sensor and harzburgite samples of San508. Colour represents multiples of uniform distribution (MUD).

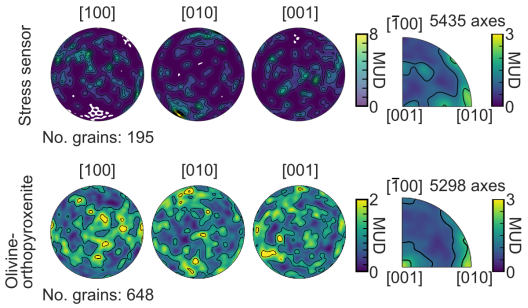

Figure B2. Pole and inverse pole figures for olivine in the stress sensor and olivine-orthopyroxenite samples of San502. Colour represents multiples of uniform distribution (MUD).

Figure B2 contains the equivalent pole figures and inverse pole figures for olivine in both the stress sensor and the olivine-orthopyroxenite sample in experiment San502. In all pole figures olivine displays no discernible CPO. For the stress sensor, this lack of CPO may in part be due to the low number of grains available for analysis (195). However, this reasoning does not apply to the olivine in the olivine orthopyroxenite, for which 648 grains were measured. Despite the lack of CPOs, the presence of subgrain boundaries within olivine in both the stress sensor and the mixture implies that dislocations were active during deformation. Similar to San508, olivine in both samples exhibits subgrain boundaries with misorientation axes clustered approximately parallel to [001] and [010]. Unlike San508, the olivine in the olivine orthopyroxenite also contains subgrain boundaries with misorientation axes clustered parallel to [100]. These latter subgrain boundaries can represent tilt boundaries composed of (010)[001] edge dislocations. In both cases the cluster parallel to [001] is secondary in strength. Without crystal preferred orientations it is not possible to identify the exact slip system, however the misorientation axes indicate that (010)[100] is

not likely to be the dominant slip system and therefore the dominant Burgers vector was likely [001].

Figure B3 presents pole and inverse pole figures for orthopyroxene in San502 and San508. In both cases, misorientation axes of subgrain boundaries are predominantly clustered around [010], indicating that the subgrain boundaries are formed by dislocations on the (001)[100] and/or (100)[001] slip systems. Both samples also exhibit a submaximum of misorientation axes parallel to [001], indicating a subpopulation of subgrain boundaries composed of dislocations on the (010)[100] and/or (100)[010] slip systems. In sample San502, both [100] and [010] axes are clustered parallel to σ_1 with [001] axes in a girdle normal to σ_1. These grain orientations indicate that [001] was the dominant slip direction in this sample and, in combination with the interpretations from misorientation axes of subgrain boundaries, suggest that (100)[001] is the dominant slip system. In sample San508, [100] axes are randomly oriented, [010] axes cluster parallel to σ_1, and [001] axes form a girdle normal to σ_1. These grain orientations suggest that (010)[001] was the slip system providing the greatest contribution to grain rotations. Overall, these results indicate that [001] was the dominant Burgers vector in orthopyroxene in these experiments, which is consistent with previous observations of experimental and natural samples (Jung et al., 2010).

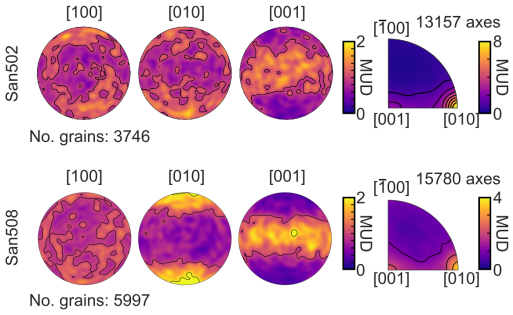

Figure B3. Pole figures and inverse pole figures for orthopyroxene in the harzburgite sample of San508 and the olivine-orthopyroxenite sample of San502. Colour represents multiples of uniform distribution (MUD).

Acknowledgments

We are grateful for the expertise and technical assistance of Haiyan Chen at beamline 6-B,M-B at the Advanced Photon Source. Use of the Advanced Photon Source, an Office of Science User Facility operated for the U.S. Department of Energy (DOE) by Ar-

gonne National Laboratory, was supported by U.S. DOE under Contract No. DE-AC02-06CH11357. Experiments were run at the Argonne National Laboratory under general user proposals (GUP) 55176 and 68700. We are grateful for the assistance of Jamie Long and James King with sample preparation and Jon Wells for thin-section preparation. Leif Tolke and Amanda Dillman generously provided sample materials. This work was supported by NERC Environmental Research DTP grant NE/L002612/1, University of Oxford, to R.M.G., National Science Foundation grants EAR-1806791 to K.M.K. and EAR-2022433 to L.N.H., a UK Research and Innovation Future Leaders Fellowship [grant number MR/V021788/1] to D.W., and a grant from the Netherlands Organisation for Scientific Research, User Support Programme Space Research [grant number ALWGO.2018.038] to D.W. Support for EBSD data collection at the Marine Biological Laboratory was provided by National Science Foundation grant EAR-2003389 to A.J.C. Portions of this work were performed under the auspices of the U.S. Department of Energy by Lawrence Livermore National Laboratory under Contract DE-AC52-07NA27344. LLNL-JRNL-851361.

References

Abramson, E., Brown, J. M., Slutsky, L. J., & Zaug, J. (1997). The elastic constants of san carlos olivine to 17 gpa. *Journal of Geophysical Research: Solid Earth*, *102*, pp. 12253-12263. doi: https://doi.org/10.1029/97JB00682

Ambrose, T. K., Wallis, D., Hansen, L. N., Waters, D. J., & Searle, M. P. (2018). Controls on the rheological properties of peridotite at a palaeosubduction interface: A transect across the base of the oman–uae ophiolite. *Earth and Planetary Science Letters*, *491*, pp. 193-206. doi: https://doi.org/10.1016/j.epsl.2018.03.027

Angel, R. J., & Hugh-Jones, D. A. (1994). Equations of state and thermodynamic properties of enstatite pyroxenes. *Journal of Geophysical Research: Solid Earth*, *99*, pp.19777–19783. doi: https://doi.org/10.1029/94JB01750

Ashby, M. F. (1970). The deformation of plastically non-homogeneous materials. *Philosophical Magazine*, *21*, pp. 399-424. doi: https://doi.org/10.1080/14786437008238426

Bachmann, F., Hielscher, R., & Schaeben, H. (2010). Texture analysis with mtex – free and open source software toolbox. *Solid State Phenomena*, *160*, pp. 63-68. doi: https://doi.org/10.4028/www.scientific.net/SSP.160.63

Bai, Q., Mackwell, S. J., & Kohlstedt, D. L. (1991). High-temperature creep of olivine single crystals 1. mechanical results for buffered samples. *Journal of Geophysical Research:*

Solid Earth, *96*, pp. 2441-2463. doi: https://doi.org/10.1029/90JB01723

Behr, W. M., & Platt, J. P. (2011). A naturally constrained stress profile through the middle crust in an extensional terrane. *Earth and Planetary Science Letters*, *303*, pp. 181-192. doi: https://doi.org/10.1016/j.epsl.2010.11.044

Boutonnet, E., Leloup, P. H., Sassier, C., Gardien, V., & Ricard, Y. (2013). Ductile strain rate measurements document long-term strain localization in the continental crust. *Geology*, *41*, pp. 819–822. doi: https://doi.org/10.1130/G33723.1

Burnley, P. C., & Kaboli, S. (2019). Elastic plastic self-consistent (epsc) modeling of san carlos olivine deformed in a d-dia apparatus. *American Mineralogist*, *104*, pp. 276-281. doi: https://doi.org/10.2138/am-2019-6666

Bystricky, M., Heidelbach, F., & Mackwell, S. (2006). *Large-strain deformation and strain partitioning in polyphase rocks: Dislocation creep of olivine–magnesiowüstite aggregates*, *427*, pp. 115-132. doi: https://doi.org/10.1016/j.tecto.2006.05.025

Campbell, L. R., & Menegon, L. (2019). Transient high strain rate during localized viscous creep in the dry lower continental crust (lofoten, norway). *Journal of Geophysical Research: Solid Earth*, *124*, pp. 10240-10260. doi: https://doi.org/10.1029/2019JB018052

Carter, N. L., & Ave'Lallemant, H. G. (1970). High temperature flow of dunite and peridotite. *Geological Society of America Bulletin*, *81*, pp. 2181–2202. doi: https://doi.org/10.1130/0016-7606(1970)81[2181:HTFODA]2.0.CO;2

Chai, M., Brown, J. M., & Slutsky, L. J. (1997). The elastic constants of an aluminous orthopyroxene to 12.5 gpa. *Journal of Geophysical Research: Solid Earth*, *102*, pp. 14779-14785. doi: https://doi.org/10.1029/97JB00893

Christensen, N. I. (1966). Elasticity of ultrabasic rocks. *Journal of Geophysical Research (1896-1977)*, *71*, pp. 5921-5931. doi: https://doi.org/10.1029/JZ071i024p05921

Cross, A. J., & Skemer, P. (2017). Ultramylonite generation via phase mixing in high-strain experiments. *Journal of Geophysical Research: Solid Earth*, *112*, pp. 1744-1759. doi: https://doi.org/10.1002/2016JB013801

Deer, W., Howie, R. A., & Zussman, J. (1988). *An introduction to the rock-forming minerals*. London, UK: Longman.

Dixon, N. A., & Durham, W. B. (2018). Measurement of activation volume for creep of dry olivine at upper-mantle conditions. *Journal of Geophysical Research: Solid Earth*, *123*, pp. 8459-8473. doi: https://doi.org/10.1029/2018JB015853

Druiventak, A., Trepmann, C. A., Renner, J., & Hanke, K. (2011). Low-temperature plasticity of olivine during high stress deformation of peridotite at lithospheric conditions — an experimental study. *Earth and Planetary Science Letters*, *311*, pp. 199-211. doi: https://doi.org/10.1016/j.epsl.2011.09.022

Durham, W. B., Goetze, C., & Blake, B. (1977). Plastic flow of oriented single crystals of olivine: 2. observations and interpretations of the dislocation structures. *Journal of Geophyiscal Research*, *82*, pp. 5755-5770. doi: https://doi.org/10.1029/JB082i036p05755

Durham, W. B., Mei, S., Kohlstedt, D., Wang, L., & Dixon, N. (2009). New measurements of activation volume in olivine under anhydrous conditions. *Physics of the Earth and Planetary Interiors*, *172*, pp. 67-73. doi: https://doi.org/10.1016/j.pepi.2008.07.045

Durham, W. B., Weidner, D. J., Karato, S.-I., & Wang, Y. (2002). New developments in deformation experiments at high pressure. *Reviews in Mineralogy Geochemistry*, *51*, pp. 21–49. doi: https://doi.org/10.2138/gsrmg.51.1.21

Evans, B., Renner, J., & Hirth, G. (2001). A few remarks on the kinetics of static grain growth in rocks. *International Journal of Earth Sciences*, *90*, pp. 88-103. doi: https://doi.org/10.1007/s005310000150

Gaboriaud, R. J., Darot, M., Gueguen, Y., & Woirgard, J. (1981). Dislocations in olivine indented at low temperatures. *Physics and Chemistry of Minerals*, *7*, pp. 100-104. doi: https://doi.org/10.1007/BF00309460

Girard, J., & ichiro Karato, S. (2022). An experimental study of evolution of strength of olivine aggregates under upper mantle conditions using in-situ synchrotron x-ray..

Goddard, R. M., Hansen, L. N., Wallis, D., Stipp, M., III, C. W. H., Kumamoto, K. M., & Kohlstedt, D. L. (2020). A subgrain-size piezometer calibrated for ebsd. *Geophysical Research Letters*, *47*. doi: https://doi.org/10.1029/2020GL090056

Goddard, R. M., Kumamoto, K. M., Hansen, L. N., Wallis, D., Cross, A. J., & Thom, C. A. (2023). *D-dia: Subgrain-size piezometry* [dataset]. OSF. doi: https://doi.org/10.17605/OSF.IO/UATJG

Handy, M. R. (1990). The solid-state flow of polymineralic rocks. *Journal of Geophysical Research: Solid Earth*, *95*, pp. 8647-8661. doi: https://doi.org/10.1029/JB095iB06p08647

Handy, M. R. (1994). Flow laws for rocks containing two non-linear viscous phases: A phenomenological approach. *Journal of Structural Geology*, *16*, pp. 287-301. doi: https://doi.org/10.1016/0191-8141(94)90035-3

Hansen, L. N., Kumamoto, K. M., Thom, C. A., Wallis, D., Durham, W. B., Goldsby, D. L., ... Kohlstedt, C. D. M. . D. L. (2019). Low-temperature plasticity in olivine: Grain size, strain hardening, and the strength of the lithosphere. *Journal of Geophysical Research: Solid Earth*, *124*, pp. 5427–5449. doi: https://doi.org/10.1029/2018JB016736

Hansen, L. N., & Warren, J. M. (2015). Quantifying the effect of pyroxene on deformation of peridotite in a natural shear zone. *Journal of Geophysical Research: Solid Earth*, *120*, pp. 717-2738. doi: https://doi.org/10.1002/2014JB011584

Hansen, L. N., Zhao, Y.-H., Zimmerman, M. E., & Kohlstedt, D. L. (2014). Protracted fabric evolution in olivine: Implications for the relationship among strain, crystallographic fabric, and seismic anisotropy. *Earth and Planetary Science Letters*, *387*, pp. 157-168. doi: https://doi.org/10.1016/j.epsl.2013.11.009

Hiraga, T., Tachibana, C., Ohashi, N., & Sano, S. (2010). Grain growth systematics for forsterite ± enstatite aggregates: Effect of lithology on grain size in the upper mantle. *Earth and Planetary Science Letters*, *291*, pp. 10-20. doi: https://doi.org/10.1016/j.epsl.2009.12.026

Huang, Y., Humphreys, F., & Ferry, M. (2000). Hot deformation and annealing of cube oriented aluminium single crystals. *Materials Science and Technology*, *16*, pp. 1367-1371. doi: https://doi.org/10.1179/026708300101507271

Idrissi, H., Bollinger, C., Boioli, F., Schryvers, D., & Cordier, P. (2016). Low-temperature plasticity of olivine revisited with in situ tem nanomechanical testing. *Science Advances*, *2*, e1501671. doi: https://doi.org/10.1126/sciadv.1501671

III, C. W. H., & Kronenberg, A. K. (2010). Accurate differential stress measurement using the molten salt cell and solid salt assemblies in the griggs apparatus with applications to strength, piezometers and rheology. *Tectonophysics*, *494*, pp.17-31. doi: https://doi.org/10.1016/j.tecto.2010.08.001

Isaak, D. G. (1992). High-temperature elasticity of iron-bearing olivines. *Journal of Geophysical Research: Solid Earth*, *97*, pp. 1871-1885. doi: https://doi.org/10.1029/91JB02675

Jung, H., Park, M., Jung, S., & Lee, J. (2010). Lattice preferred orientation, water content, and seismic anisotropy of orthopyroxene. *Journal of Earth Science*, *21*, pp. 555–568. doi: https://doi.org/10.1007/s12583-010-0118-9

Karato, S. (2012). *Deformation of earth materials: An introduction to the rheology of solid earth*. Cambridge University Press.

Karato, S. (2021). A theory of inter-granular transient dislocation creep: Implications for the geophysical studies on mantle rheology. *Journal of Geophysical Research: Solid Earth*, *126*. doi: https://doi.org/10.1029/2021JB022763

Karato, S., Toriumi, M., & Fujii, T. (1980). Dynamic recrystallization of olivine single crystals during high temperature creep. *Geophysical Research Letters*, *7*, pp. 649-652. doi: https://doi.org/10.1029/GL007i009p00649

Kidder, S., Hirth, G., Avouac, J. P., & Behr, W. (2016). The influence of stress history on the grain size and microstructure of experimentally deformed quartzite. *Journal of Structural Geology*, *83*, pp.194-206. doi: https://doi.org/10.1016/j.jsg.2015.12.004

Kohlstedt, D. L., & Weathers, M. S. (1980). Deformation-induced microstructures, paleopiezometers, and differential stresses in deeply eroded fault zones. *Journal of Geophysical Research: Solid Earth*, *85*, pp. 6269-6285. doi: https://doi.org/10.1029/JB085iB11p06269

Kumazawa, M., & Anderson, O. L. (1969). Elastic moduli, pressure derivatives, and temperature derivatives of single-crystal olivine and single-crystal forsterite. *Journal of Geophysical Research*, *74*, pp. 5961-5972. doi: https://doi.org/10.1029/JB074i025p05961

Li, L., Addad, A., Weidner, D., Long, H., & Chen, J. (2007). High pressure deformation in two-phase aggregates. *Tectonophysics*, *439*, pp. 107-117. doi: https://doi.org/10.1016/j.tecto.2007.04.004

Li, L., Weidner, D., Raterron, P., Chen, J., Vaughan, M., Mei, S., & Durham, B. (2006). Deformation of olivine at mantle pressure using the d-dia. *European Journal of Mineralogy*, *18*, pp. 7-19. doi: https://doi.org/10.1127/0935-1221/2006/0018-0007

Linckens, J., & Tholen, S. (2021). Formation of ultramylonites in an upper mantle shear zone, erro-tobbio, italy. *Minerals*, *11*. doi: https://doi.org/10.3390/min11101036

Luton, M., & Sellars, C. (1969). Dynamic recrystallization in nickel and nickel-iron alloys during high temperature deformation. *Acta Metallurgica*, *17*, pp. 1033-1043. doi: https://doi.org/10.1016/0001-6160(69)90049-2

Maitland, T., & Sitzman, S. (2007). Scanning microscopy for nanotechnology: Techniques and applications. In (p. pp. 41-75). Springer.

Mao, Z., Fan, D., Lin, J.-F., Yang, J., Tkachev, S. N., Zhuravlev, K., & Prakapenka, V. B. (2015). Elasticity of single-crystal olivine at high pressures and temperatures. *Earth and Planetary Science Letters*, *426*, pp. 204-215. doi: https://doi.org/10.1016/j.epsl

.2015.06.045

Mei, S., Suzuki, A. M., Kohlstedt, D. L., Dixon, N. A., & Durham, W. B. (2010). Experimental constraints on the strength of the lithospheric mantle. *Journal of Geophysical Research: Solid Earth*, *115*, Q08012. doi: https://doi.org/10.1029/2009JB006873

Menegon, L., Campbell, L., Mancktelow, N., Camacho, A., Wex, S., Papa, S., ... Pennacchioni, G. (2021). The earthquake cycle in the dry lower continental crust: insights from two deeply exhumed terranes (musgrave ranges, australia and lofoten, norway). *Philosophical transactions of the Royal Society A*, *379*, p. 20190416. doi: https://doi.org/10.1098/rsta.2019.0416

Meyers, C., Kohlstedt, D., & Zimmerman, M. (2017, December). Densification and grain growth in polycrystalline olivine rocks synthesized by evacuated hot-pressing. In *Agu fall meeting abstracts.*

Nicolas, A. (1978). Stress estimates from structural studies in some mantle peridotites. *Philosophical Transactions of the Royal Society of London. Series A, Mathematical and Physical Sciences*, *288*, pp. 49–57. doi: https://doi.org/10.1098/rsta.1978.0005

O'Haver, T. (2018). Pragmatic introduction to signal processing 2019: Applications in scientific measurement. *Independently Published*.

Qin, Y., Götz, G., & Blum, W. (2003). Subgrain structure during annealing and creep of the cast martensitic cr-steel g-x12crmowvnbn 10-1-1. *Materials Science and Engineering: A*, *341*, pp. 211-215. doi: https://doi.org/10.1016/S0921-5093(02)00215-0

Raleigh, C. B., & Kirby, S. H. (1970). Creep in the upper mantle. *Mineralogical Society of America Special Paper*, *180*, pp. 113-121.

Raterron, P., Fraysse, G., Girard, J., & III, C. W. H. (2016). Strength of orthoenstatite single crystals at mantle pressure and temperature and comparison with olivine. *Earth and Planetary Science Letters*, *450*, pp. 326-336. doi: https://doi.org/10.1016/j.epsl.2016.06.025

Ross, J. V., Lallemant, H. G. A., & Carter, N. L. (1980). Stress dependence of recrystallized-grain and subgrain size in olivine. *Tectonophysics*, *70*, pp. 39-61. doi: https://doi.org/10.1016/0040-1951(80)90020-7

Sachs, G. Z. (1928). The plastic deformation mode of polycrystals. *Zeitschrift des Vereines Deutscher Ingenieure*.

Servi, I. S., Norton, J. T., & Grant, N. J. (1952). Some observations of subgrain formation during creep in high purity aluminum. *The Journal of The Minerals, Metals Materials*

Society, *4*, pp. 965–971. doi: https://doi.org/10.1007/BF03397754

Shimizu, I. (2008). Theories and applicability of grain size piezometers: The role of dynamic recrystallization mechanisms. *Journal of Structural Geology*, *30*, pp. 899-917. doi: https://doi.org/10.1016/j.jsg.2008.03.004

Silber, R. E., Girard, J., & ichiro Karato, S. (2022). Effects of pressure on diffusion creep in wet olivine aggregates. *Physics of the Earth and Planetary Interiors*, *324*, pp. 106840. doi: https://doi.org/10.1016/j.pepi.2022.106840

Singh, A. K., Balasingh, C., kwang Mao, H., Hemley, R. J., & Shu, J. (1998). Analysis of lattice strains measured under nonhydrostatic pressure. *Journal of Applied Physics*, *83*, pp. 7567–7575. doi: https://doi.org/10.1063/1.367872

Skemer, P., Warren, J. M., Kelemen, P. B., & hirth, G. (2010). Microstructural and rheological evolution of a mantle shear zone. *Journal of Petrology*, *51*, pp. 43-53. doi: https://doi.org/10.1093/petrology/egp057

Smith, C. (1948). Zener pinning. *Transactions of the Metallurgical Society of AIME*, *175*, pp. 15–51.

Soleymani, H., Kidder, S., Hirth, G., & Garapić, G. (2020). The effect of cooling during deformation on recrystallized grain-size piezometry. *Geology*, *46*, pp. 531–535. doi: https://doi.org/10.1130/G46972.1

Speciale, P., Tokle, L., & Behr, W. (2022). Feldspar and orthopyroxene piezometers constrained using quartz–feldspar and olivine–orthopyroxene mineral pairs from natural mylonites. *Journal of Structural Geology*, *154*, 104495. doi: https://doi.org/10.1016/j.jsg.2021.104495

Stenvall, C. A., Åke Fagereng, & Diener, J. F. A. (2019). Weaker than weakest: On the strength of shear zones. *Geophysical Research Letters*, *46*, 7404-7413.

Stipp, M., & Tullis, J. (2003). The recrystallized grain size piezometer for quartz. *Geophysical Research Letters*, *30*. doi: https://doi.org/10.1029/2003GL018444

Tasaka, M., Zimmerman, M. E., Kohlstedt, D. L., Stünitz, H., & Heilbronner, R. (2017). Rheological weakening of olivine + orthopyroxene aggregates due to phase mixing: Part 2. microstructural development. *Journal of Geophysical Research: Solid Earth*, *122*, pp. 7597-7612. doi: https://doi.org/10.1002/2017JB014311

Toriumi, M. (1979). Relation between dislocation density and subgrain size of naturally deformed olivine in peridotites. *Contributions to Mineralogy and Petrology*, *68*, pp. 181–186. doi: https://doi.org/10.1007/BF00371899

Trepmann, C. A., & Seybold, L. (2019). Deformation at low and high stress-loading rates. *Geoscience Frontiers*, *10*, pp. 43-54. doi: https://doi.org/10.1016/j.gsf.2018.05.002

Tullis, J. A. (1979). High temperature deformation of rocks and minerals. *Tectonophysics*, *17*, pp. 1137-1154. doi: https://doi.org/10.1029/RG017i006p01137

Twiss, R. (1977). Stress in the earth. In (p. pp. 227-244). Birkhäuser, Basel. doi: https://doi.org/10.1007/978-3-0348-5745-1_13

Twiss, R. (1986). Variable sensitivity piezometric equations for dislocation density and subgrain diameter and their relevance to olivine and quartz. In B. E. Hobbs & H. C. Heard (Eds.), *Mineral and rock deformation:laboratory studies* (p. pp. 247–263). AGU Geophysical Monographs.

van der Wal, D., Chopra, P., Drury, M., & Gerald, J. (1993). Relationships between dynamically recrystallized grain size and deformation conditions in experimentally deformed olivine rocks. *Geophysical Research Letters*, *20*, pp. 1479–1482. doi: https://doi.org/10.1029/93GL01382

Wallis, D., Hansen, L., Tasaka, M., Kumamoto, K., Parsons, A., Lloyd, G., … Wilkinson, A. (2019). The impact of water on slip system activity in olivine and the formation of bimodal crystallographic preferred orientations. *Earth and Planetary Science Letters*, *508*, pp. 51-61. doi: https://doi.org/10.1016/j.epsl.2018.12.007

Wallis, D., Hansen, L. N., Kumamoto, K. M., Thom, C. A., Plümper, O., Ohl, M., … Wilkinson, A. J. (2020). Dislocation interactions during low-temperature plasticity of olivine and their impact on the evolution of lithospheric strengthearth and planetary science letters. *Earth and Planetary Science Letters*, *543*, 116349. doi: https://doi.org/10.1016/j.epsl.2020.116349

Wang, Y., Durham, W. B., Getting, I. C., & Weidner, D. J. (2003). The deformation-dia: A new apparatus for high temperature triaxial deformation to pressures up to 15 gpa. *REview of Scientific Instruments*, *74*, pp. 3002–3011. doi: https://doi.org/10.1063/1.1570948

Wang, Y., Hilairet, N., Nishiyama, N., Yahata, N., Tsuchiya, T., Morard, G., & Fiquet, G. (2013). High-pressure, high-temperature deformation of cageo3 (perovskite)±mgo aggregates: Implications for multiphase rheology of the lower mantle. *Geochemistry, Geophysics, Geosystems*, *14*, pp. 3389-3408. doi: https://doi.org/10.1002/ggge.20200

Warren, J. M., & Hirth, G. (2006). Grain size sensitive deformation mechanisms in naturally deformed peridotites. *Earth and Planetary Science Letters*, *248*, 438-450. doi: https://

1110 doi.org/10.1016/j.epsl.2006.06.006

1111 Weidner, D. J., Vaughan, M. T., Wang, L., Long, H., Li, L., Dixon, N. A., & Durham, W. B.
1112 (2010). Precise stress measurements with white synchrotron x rays. *Review of Scientific*
1113 *Instruments*, *81*. doi: https://doi.org/10.1063/1.3263760

1114 White, S. (1979). Contributions to mineralogy and petrology. *Contributions to Mineralogy*
1115 *and Petrology*, *70*, pp. 193-202. doi: https://doi.org/10.1007/BF00374448